CHILES VI

Bird, J. Blue; Davis, J.; Luber, N.; van Gorkom, J. H.; Wilcots, E.; Pisano, D. J.; Gim, H. B.; Momjian, E.; Fernandez, X.; Hess, K. M.

Published in:
Monthly Notices of the Royal Astronomical Society

DOI:
10.1093/mnras/stz3357

Publication date:
2020

Monthly Notices of the ROYAL ASTRONOMICAL SOCIETY

MNRAS **492,** 153–176 (2020) doi:10.1093/mnras/stz3357
Advance Access publication 2019 December 3

CHILES VI: H I and H α observations for $z < 0.1$ galaxies; probing H I spin alignment with filaments in the cosmic web

J. Blue Bird,[1★] J. Davis,[2★] N. Luber,[3,4] J. H. van Gorkom,[1] E. Wilcots,[2] D. J. Pisano,[3,4,5] H. B. Gim,[6,7] E. Momjian,[8] X. Fernandez,[9] K. M. Hess,[10,11] D. Lucero,[12] R. Dodson,[13] K. Vinsen,[13] A. Popping,[13,14] A. Chung,[15] K. Kreckel,[16] J. M. van der Hulst[11] and M. Yun[6]

[1]*Department of Astronomy, Columbia University, 550 West 120th Str, New York, NY 10027, USA*
[2]*Department of Astronomy, University of Wisconsin – Madison, 475 N Charter Str, Madison, WI 53706, USA*
[3]*Department of Physics and Astronomy, West Virginia University, PO Box 6315, Morgantown, WV 26506, USA*
[4]*Center for Gravitational Waves and Cosmology, West Virginia University, Chestnut Ridge Research Building, Morgantown, WV 26505, USA*
[5]*Adjunct Astronomer at Green Bank Observatory, Green Bank, WV 24944, USA*
[6]*Department of Astronomy, University of Massachusetts, Amherst, MA 01003, USA*
[7]*School of Earth and Space Exploration, Arizona State University, 781 Terrace Mall, Tempe, AZ 85287 USA*
[8]*National Radio Astronomy Observatory, PO Box 0, Socorro, NM 87801, USA*
[9]*Department of Physics and Astronomy, Rutgers, The State University of New Jersey, Piscataway, NJ 08854-8019, USA*
[10]*ASTRON, the Netherlands Institute for Radio Astronomy, Postbus 2, Dwingeloo NL-7900AA, the Netherlands*
[11]*Kapteyn Astronomical Institute, University of Groningen, Landleven 12, 9747 AD, Groningen, the Netherlands*
[12]*Department of Physics, Virginia Tech, 850 West Campus Drive, Blacksburg, VA 24061, USA*
[13]*International Centre for Radio Astronomy Research, The University of Western Australia, Crawley, WA 6009, Australia*
[14]*Australian Research Council, Centre of Excellence for All-sky Astrophysics (CAASTRO), Australia*
[15]*Department of Astronomy, Yonsei University, 50 Yonsei-ro, Seodaemun-gu, Seoul 03722, Korea*
[16]*Max Planck Institute for Astronomy, Knigstuhl 17, D-69117 Heidelberg, Germany*

Accepted 2019 November 27. Received 2019 November 27; in original form 2019 September 11

ABSTRACT

We present neutral hydrogen (H I) and ionized hydrogen (H α) observations of 10 galaxies out to a redshift of 0.1. The H I observations are from the first epoch (178 h) of the COSMOS H I Large Extragalactic Survey (CHILES). Our sample is H I biased and consists of 10 late-type galaxies with H I masses that range from 1.8×10^7 $M_\odot$ to 1.1×10^{10} $M_\odot$. We find that although the majority of galaxies show irregularities in the morphology and kinematics, they generally follow the scaling relations found in larger samples. We find that the H I and H α velocities reach the flat part of the rotation curve. We identify the large-scale structure in the nearby CHILES volume using DisPerSE with the spectroscopic catalogue from SDSS. We explore the gaseous properties of the galaxies as a function of location in the cosmic web. We also compare the angular momentum vector (spin) of the galaxies to the orientation of the nearest cosmic web filament. Our results show that galaxy spins tend to be aligned with cosmic web filaments and show a hint of a transition mass associated with the spin angle alignment.

Key words: galaxy: evolution – galaxy: formation – galaxy: kinematics and dynamics – large-scale structure of the Universe.

1 INTRODUCTION

In the last decade, tremendous progress has been made in our understanding of structure formation in the Universe. Simulations of dark matter show that structures develop over time forming the large-scale structure of the Universe – the so-called cosmic web consisting of walls, filaments, and voids. Observations show that galaxies lie in this interconnected cosmic web and that stars trace the dark matter. However, how galaxies grow and evolve is less well understood.

Ongoing infall of gas from the intergalactic medium is thought to be important for the growth of galaxies, with cold gas accretion from the cosmic web likely a dominant factor (Sánchez Almeida et al. 2014). Simulations and models highlight physical processes that may be relevant in studying large-scale environments. Theorists

★ E-mail: julia@astro.columbia.edu (JBB); jdavis@astro.wisc.edu (JD)

distinguish two modes of gas infall: 'hot mode' accretion where gas gets shock heated to high temperatures and then slowly cools and settles in a disc, and 'cold mode' accretion where much cooler gas flows along filaments directly into the disc. 'Cold mode' accretion is a favourable scenario for gas accretion on to galaxies and simulations make very specific predictions about its dependence on galaxy mass, environment, and redshift (Kereš et al. 2005). Recently, Aragon Calvo, Neyrinck & Silk (2019) proposed the halting of cold gas accretion through cosmic web detachment. In this picture, galaxies accrete cold gas from the cosmic web until they enter regions of crossing velocity streams, including regions near large filament backbones. These interactions detach galaxies from the cosmic web and sever their cold gas supply, quenching star formation. As the interaction between galaxies and the neutral hydrogen (H I) reservoir in filaments is poorly constrained, more work is needed to confidently measure the influence large-scale structure has on galaxy evolution.

There has been a growing number of methods to quantify large-scale environment; Libeskind et al. (2018) provide a review and a comparison of different methods. Methods such as Discrete Persistent Structure Extractor (DisPerSE; Sousbie 2011), a scale-free topological algorithm that uses Morse theory and Delaunay tessellations, are used to characterize the large-scale distribution of galaxies. It is by now well established that galaxy properties, such as stellar mass, colour-type and star formation rate (SFR), show dependence on location in large-scale environment (Chen et al. 2017; Kuutma, Tamm & Tempel 2017; Malavasi et al. 2017; Kraljic et al. 2018; Laigle et al. 2018; Luber et al. 2019). More recently, H I as a function of distance to cosmic web filaments has been investigated with conflicting results (Kleiner et al. 2017; Crone Odekon et al. 2018). In addition to location, there are predictions about the orientation of galaxies with respect to large-scale structure (Porciani, Dekel & Hoffman 2002; Codis, Pichon & Pogosyan 2015). A key prediction is that low-mass galaxies tend to align their angular momentum vector (spin) with their nearby filament, while high-mass galaxies tend to have their spin perpendicular to their nearby filament. This is seen in both dark matter simulations for haloes (Ganeshaiah Veena et al. 2018; Wang et al. 2018) and hydrodynamic simulations for galaxies (Codis et al. 2018; Kraljic, Dave & Pichon 2019). Observational studies of galaxy spin-filament alignments show mixed results. Hints of spin alignment for galaxies have been identified by Tempel, Stoica & Saar (2013), Tempel & Libeskind (2013), Pahwa et al. (2016), Chen et al. (2019), and Welker et al. (2019), while Krolewski et al. (2019) find no evidence for alignment. The next generation of H I surveys, such as the COSMOS H I Large Extragalactic Survey (CHILES), will provide unique observations to compare to these studies and predictions.

While ongoing infall of gas from the intergalactic medium is thought to be important for the growth of galaxies, observational evidence of accretion remains challenging to obtain. Due to the intrinsic faintness of H I 21-cm emission, it has been difficult to probe beyond a redshift of $z \sim 0.1$ without prohibitively long integration times. Large single-dish radio surveys such as HIPASS (Barnes et al. 2001) and ALFALFA (Giovanelli et al. 2005) have compiled a large number of H I-detected galaxies, but only to a redshift of $z \sim 0.06$, and with relatively low angular resolution. At higher resolution, targeted interferometric surveys of varying galaxy type and environment such as WHISP (Van der Hulst, van Albada & Sancisi 2001), THINGS (Walter et al. 2008), VIVA (Chung et al. 2009), HALOGAS (Heald et al. 2011), Little THINGS (Hunter et al. 2012), and VGS (Kreckel et al. 2012) have uncovered numerous interesting H I features potentially linked to formation or accretion processes. From these observations (see Sancisi et al. 2008 for a review), we have learned much about H I distributions and kinematics and how we might infer the presence of accretion. Accretion phenomena become evident in the outskirts and extraplanar regions of spiral galaxy discs, requiring deep 21-cm emission investigations to search for lower column density and/or anomalous velocity range gas. With long integration times, the CHILES survey is beginning to probe this regime beyond the most local galaxies.

CHILES is an H I survey using the upgraded Karl G. Jansky Very Large Array (VLA). For the first time, we are imaging the H I distribution and kinematics in a single pointing of continuous redshift range $0 < z < 0.45$. CHILES will measure the H I gas reservoir over a substantial look-back time and provide H I content, morphology, and kinematics for a wide range of stellar masses and environments. CHILES will produce H I images of at least 300 galaxies across the entire redshift range, with a linear resolution of 350 pc, 19 kpc, and 42 kpc at $z = 0.03$, $z = 0.20$, and $z = 0.45$, respectively. The survey will be able to detect at the highest redshift 3.0×10^{10} $M_{\odot}$ at 5σ, assuming a 150 km s^{-1} profile width. The 40 arcmin $\times$ 40 arcmin pointing in the COSMOS field (Scoville et al. 2007) is chosen such that it has no strong continuum sources. The COSMOS field is ideal for a survey like this because of the wealth of ancillary data.

In this paper, we present results for 10 galaxies out to a redshift of 0.1, from the first epoch of the CHILES survey. At 178 h, this is a unique amount of observing time as nearby galaxies are typically observed for only a few hours resulting in column density sensitivities an order of magnitude lower at similar resolution. We utilize this first epoch of data as a science verification study for the CHILES survey. Our results reveal irregularities in the morphologies and kinematics in most of the sample. Our results show a tendency of galaxy spins to be aligned with cosmic web filaments and possibly the existence of a transition mass where the alignment changes.

In addition to the H I data, we study ionized gas kinematics with optical long-slit data obtained from the Southern African Large Telescope (SALT). Observations of optical emission lines trace population I stars, particularly H II regions associated with star-forming regions in the galactic disc. These lines are a good tracer of the overall circular motion of the disc, given that they have small velocity dispersion compared to the rotation velocity. In this paper, we examine the structural relation of H I and H α discs with rotation curves of H α in the inner regions and with H I in the outer regions. The results reveal that the flat part of the rotation curve is reached for the H α data, along with disturbed kinematics due to non-circular motion in the inner region of one of the irregular galaxies in our sample.

This paper is organized as follows. In Section 2, we outline the observations and data reduction for H I and H α. In Section 3, we describe the data analysis, sample properties, individual galaxies, and the derivations of the galaxy environments. In Section 4, we analyse the stellar, H I and H α content including H I gas fraction, H I deficiency, H I size–mass relation, H I and H α line width comparison, and H I and H α baryonic Tully–Fisher relation. In Section 5, we discuss the H I morphology and kinematics as well as the H I properties as a function of distance and orientation to the cosmic web. Section 6 covers the conclusion. In the Appendix, we present figures for the individual galaxies.

Throughout this paper, we use J2000 coordinates, velocities in the optical convention, and a barycentric reference frame. This paper

Table 1. CHILES observation details for our sample.

Survey epoch	Epoch 1
Observation date	2013–2014
Array configuration	VLA-B
Integration (h)	178
Bandpass and flux density scale calibrator	3C286
Phase calibrator	J0943–0819
Frequency coverage (MHz)	1300–1411
Redshift range	0.0068–0.0930
Synthesized beam (arcsec)	6.4×4.7^{b} – 6.8×5.1^{c}
Frequency resolution (kHz)[a]	62.5
Velocity resolution (km s^{-1})[a]	13.3^{b}–14.4^{c}
Spatial resolution (kpc)	0.8^{b}–10.7^{c}
rms noise (μJy beam^{-1} channel^{-1})[a]	76.0^{b}–83.0^{c}
Typical 1σ $N_{H\,I}$ (cm^{-2} channel^{-1})[a]	3.3^{b}–$4.4^{c} \times 10^{19}$

[a]*Notes*. After Hanning smoothing plus additional velocity smoothing. [b]At $z = 0.0068$. [c]At $z = 0.0930$.

adopts a flat Λ cold dark matter cosmology using $H_o = 67.3$ km s^{-1} Mpc^{-1} and $\Omega_M = 0.316$ (Planck Collaboration et al. 2018) to calculate distances and physical sizes.

2 OBSERVATIONS

We carried out a 60-h pilot study (Fernández et al. 2013) (CHILES I) of the CHILES field during the commissioning of the upgraded VLA correlator. We imaged H I in the redshift range $0 < z < 0.193$ and found 33 detections, from which we draw a sample to study with our 178-h first epoch of data. The full CHILES survey has been underway since late 2013 when observations began on the VLA. In Dodson et al. (2016) (CHILES II), we compared the suitability of different computing environments for processing a data set like CHILES. From the first 178 h, we already have dozens of H I detections, ranging from the $z < 0.1$ galaxies covered in this paper (CHILES VI), to galaxy groups at $z = 0.12$ and $z = 0.17$ in Hess et al. (2019) (CHILES IV), to the highest redshift H I detection so far at $z = 0.37$ in Fernández et al. (2016) (CHILES III). In a separate paper, Luber et al. (2019) (CHILES V) explore the use of DisPerSE to identify cosmic web filaments in the CHILES volume. For this work, we utilize the complementary multiband photometry and optical redshift information from the G10/COSMOS v05 catalogue (Andrews et al. 2017).

The 1000-h survey is divided into epochs spread over several years to make all observations in the VLA's B-configuration (see Table 1 for observation properties). Observations of the first epoch completed in 2014, totaling 178 h. The first epoch is divided into several observing sessions with varying lengths of 1–6 h. A 6-h session consists of approximately 5 h on-source and 1 h for calibration and set-up. The 480 MHz frequency span with dual-polarization is tuned to a range of 970–1450 MHz, corresponding to a redshift interval of $z = 0$–0.45. Frequency dithering is used with three settings to minimize sensitivity loss at the edge of sub-bands. The set-up includes 15 sub-bands of 32 MHz, with each sub-band having 2048 channels of 15.6 kHz (3.3 km s^{-1} at $z = 0$), which are then Hanning smoothed to 31.2 kHz (6.6 km s^{-1} at $z = 0$).

Data reduction is carried out in CASA (McMullin et al. 2007) using a modified version (1.2.0) of the NRAO continuum pipeline optimized for spectral line data. Each observing block is calibrated separately, with a combination of machine and manual flagging. All of the blocks are then imaged together using CASA and Amazon Web Services (as described in Dodson et al. 2016). Initial image cubes (with a pixel scale of 2 arcsec) are 4096×4096 pixels to include out-of-field sources that introduce side lobes through the main field of interest. These sources are modelled for cleaning. The images are made using Briggs weighting with a robustness factor of 0.8 and cleaned with 10 000 iterations to remove the side lobes. The image cubes are then scaled down to 2048×2048 pixels that include the full primary beam ($z = 0$). The continuum is subtracted in the image plane with a first-order polynomial fit. Image sub-cubes of 4 MHz are made consisting of 64 channels averaged to a 62.5 kHz frequency resolution (13.3 km s^{-1} at $z = 0$). Smaller sub-cubes with individual galaxies are cleaned down to 1σ of the rms using a box around the emission region.

Table 2. SALT observation details.

C08 ID (1)	Date (2)	Grating (3)	Slit (arcsec) (4)	V (5)	Exp. (s) (6)	$PA_{H\,\alpha}$ (deg) (7)
1213496	20160501	PG2300	1.5	19.1	800	214, 305
1180660	20160501	PG2300	1.5	17.4	600	84, 137
1197518	20160501	PG2300	1.5	19.6	1700	163, 46
1204837	20170423	PG2300	1.25	17.7	880	175
1227948	20160502	PG2300	1.5	19.6	1700	54, 290
1432731	20170424	PG1800	1.25	18.8	1600	101
1437568	20161229	PG1800	1.25	18.6	750	258, 18
969633	20170423	PG1800	1.25	18.6	1600	240
1419315	20170131	PG1800	1.25	19.8	1600	240, 283
1221696	20161229	PG1800	1.25	19.8	1600	180, 153

Notes. (1) COSMOS 08 ID; (2) observation date; (3) grating; (4) slit size; (5) V-band magnitude; (6) total exposure time per position angle; (7) H α position angles.

In this work, we focus on galaxies in the frequency range of 1300–1411 MHz that corresponds to a redshift range of $z = 0.0068$–0.0930. Overall, we achieve a mean rms of 80 μJy beam^{-1} per 62.5 kHz channel throughout our 10 image cubes, which is close to the theoretical noise. The channel resolution corresponds to 13.3 km s^{-1} at $z = 0.0068$ and 14.3 km s^{-1} at $z = 0.0930$. The final image resolution is 6.4×4.7 arcsec and 6.8×5.1 arcsec, in the $z = 0.0068$ and $z = 0.0930$ cubes, respectively. We reach 1σ column densities of 3.3×10^{19} cm^{-2} (13.3 km s^{-1} channel) at $z = 0.0068$ and 4.4×10^{19} cm^{-2} (14.3 km s^{-1} channel) at $z = 0.0930$.

2.1 SALT observation and data reduction

The optical long-slit data are obtained (see Table 2 for observation properties) with the Robert Stobie Spectrograph (RSS) on the 11-m SALT telescope between 2016 May and 2017 April under programmes 2016-1-SCI-020, 2016-2-SCI-045, and 2017-1-SCI-047 (PI: J. Davis). The 2300 line mm^{-1} volume phase holographic grating ($R \sim 4500$, velocity resolution 68 km s^{-1} for wavelength regions in this paper) with a 1.5 arcsec slit is used for galaxies up to $z = 0.067$, after which H α shifts off the CCD. The 1800 line mm^{-1} volume phase holographic grating ($R \sim 4000$, velocity resolution 71 km s^{-1} for wavelength regions in this paper) with a 1.25 arcsec slit is used for the rest of the galaxies. The narrower slit for the latter observations is selected to aid in sky subtraction, as OH line complexes become increasingly dense after ∼7000 Å. The RSS CCD has a pixel scale of 0.1267 arcsec pixel^{-1}, and we employed 2×2 binning for a pixel size of 0.2534 arcsec. Seeing at the SALT telescope site for the observations varied between ∼1 and 1.5 arcsec.

SALT is a fixed altitude telescope with its instrument payload located on a prime-focus tracker. Observations of most objects

are limited to windows averaging 50 min twice per night. With this limitation in mind, exposure times are optimized to obtain acceptable signal-to-noise ratio in the desired optical emission lines without spreading an observation over multiple nights. When possible, observations are fit into a single track to minimize sky-subtraction complications arising from changing flexure of the optical elements in the prime focus instrument payload.

When granted sufficient observing time, two slit position angles are selected for each galaxy; otherwise, one position angle (PA) is used. Primary position angles are selected to align with the major axis of the galaxy as identified in NED using *r*-band Sloan Digital Sky Survey (SDSS) isophotal or K_s values where available. However, in some cases, acquisition of galaxies within the slit required alignment with a bright star. In these cases, the slit is aligned as closely as possible to the major axis. The secondary slit position is selected to be ∼45° offset from the major axis or aligned with any potentially interesting optical features as seen in *Hubble Space Telescope* ACS images of the target galaxies.

Reduction of the SALT data is carried out using the PYSALT software, a package that implements standard PYRAF procedures for SALT imaging and spectroscopic data (Crawford et al. 2010). We note that the spectra are not flux calibrated, as observations of a flux calibrator added prohibitive amounts of observing time and are deemed unnecessary for our kinematic analysis. The two-dimensional (2D) spectra are sky-subtracted and wavelength-calibrated, with exposures combined when available, resulting in signal-to-noise ratios of ∼5–50 across the emission lines of interest. All galaxies but one exhibited H α λ6563, and seven galaxies exhibited one or more of the forbidden emission lines [N II] λ6583 and the doublet [S II] λλ6716, 6732. We note however that the sky subtraction for SALT at times leaves heavy residuals due to variable curvature in the skylines across the CCD, so often the [S II] doublet profile is damaged by intervening OH emission lines.

3 SAMPLE

Our sample of galaxies is drawn from H I detections found in the CHILES pilot survey and narrowed down to 10 galaxies within our H α observational limits on SALT. From the H I detections in the CHILES sample, galaxies with *V*-band magnitudes less than 20 and angular sizes greater than 10 arcsec are selected to ensure reasonable exposure times and sufficient spatial information for kinematic analysis. The redshift limit is set by the lowest resolution grating we are willing to use – the PG1800 ($R \sim 4000$, $v \sim 70$ km s^{-1}) – for which H α shifts off the CCD at $z = 0.35$, the presence of heavy CCD fringing effects beyond 8000 Å, and the limiting magnitude of $m_V < 20$ for reasonable exposure time. We note that, because we are using H α and H I emission, we are necessarily biased towards star-forming, gas-rich objects.

Our sample of 10 galaxies is comprised of various morphological types. They are located in a range of different environments and redshifts as shown in Fig. 1 and Table 3. The galaxy types include two dwarf irregulars (1213496 and 1180660), three irregulars (1197518, 1227948, and 1221696), three spirals (1204837, 1432731, and 1419315), and two barred spirals (1437568 and 969633). The redshift of the galaxies ranges from $z = 0.0068$–0.0930 with corresponding distances of 30–443 Mpc. The two closest galaxies (1213496 and 1180660) may be gravitationally interacting and the two farthest galaxies (1419315, 1221696) may be gravitationally interacting as well. The galaxies have H I masses that range from 1.8×10^7 to 1.1×10^{10} $M_\odot$, shown in Table 4. Half of the galaxies have H I extending nearly two to three times the optical radius, using the SDSS *r*-band isophotal major axis. One galaxy (1432731) has H I extending to nearly six times the optical radius. Most of the sample exhibits irregularities in the morphology and kinematics of their gas discs. Of the 10 galaxies, 6 have the H I PA offset from the optical PA by 30° or greater, discussed further in Section 5.1. The H I properties are given in Tables 3 and 4. Total H I intensity maps of the entire sample are shown in Fig. 2. Global H I profiles of the entire sample are shown in Fig. 3.

3.1 Stellar properties

Multiwavelength coverage from COSMOS provides data from which we determine stellar properties. Stellar masses and SFR are estimated from SED fitting on UV through IR data using the G10/COSMOS v05 catalogue (Andrews et al. 2017) with the energy balanced SED fit programme MAGPHYS (Da Cunha, Charlot & Elbaz 2008) and are shown in Table 4. None of the galaxies in our sample have stellar masses above 3.0×10^{10} $M_\odot$, the transition mass identified in observations below which galaxies are typically younger and in the assembly process (Kauffmann et al. 2003). The galaxies have stellar masses that range from 5.8×10^5 to 1.5×10^{10} $M_\odot$. The uncertainty in the stellar mass is of the order of 17 per cent, except for the smallest masses. As Da Cunha et al. (2008) note, the smallest galaxies are not well fit with their method. Comparing results with different methods suggests that stellar masses for our two smallest galaxies are highly uncertain. The highest SFR in our sample is ∼2 $M_\odot$ yr^{-1} with the majority falling below 1 $M_\odot$ yr^{-1}. The uncertainty in the SFR is of the order of 23 per cent.

The galaxies in the sample are moderately inclined at $39° < i < 72°$ with two galaxies having more face-on inclinations of 25° and 14°. The inclinations, given in Table 5, are calculated from SDSS-DR7 (Abazajian et al. 2009) *r*-band isophotal major and minor axes using the formula:

$$\sin i = \sqrt{\frac{(1-(b/a)^2)}{(1-q_o^2)}}, \quad (1)$$

where a and b are the major and minor axes, and $q_o = 0.2$ is the three-dimensional (3D) axial ratio following Huang et al. (2012).

Star-forming galaxies follow a tight correlation between their stellar mass (M_*) and SFR (Schiminovich et al. 2007), with smaller galaxies having a lower SFR. This correlation has a bimodal distribution of blue (late-type) actively star-forming galaxies and of red (early-type) galaxies with little or no current star formation. The population of galaxies shifts from blue to red near a stellar mass transition of 3×10^{10} $M_\odot$ (Kauffmann et al. 2003). In our sample of galaxies, SFR increases with increasing stellar mass (Table 4).

There is a similar bimodality in the mass dependence of the SFR per unit stellar mass. Fig. 4 shows the relation of specific star formation rate (SSFR) versus stellar mass for our sample. The blue line shows the fit to the star-forming sequence for an SDSS spectroscopic sample of galaxies using *GALEX* ultraviolet luminosities to measure the SFR (Schiminovich et al. 2007). Except for one, our sample appears to lie along the blue sequence. There is no clear trend when examined as a function of redshift. The SSFR increases with decreasing galaxy mass, implying that lower mass galaxies form a higher fraction of their stellar mass in the present time.

This bimodality is not absolute, with a green valley between the red and blue sequences. This valley consists of less active star-forming galaxies representing a combination of inactive disc

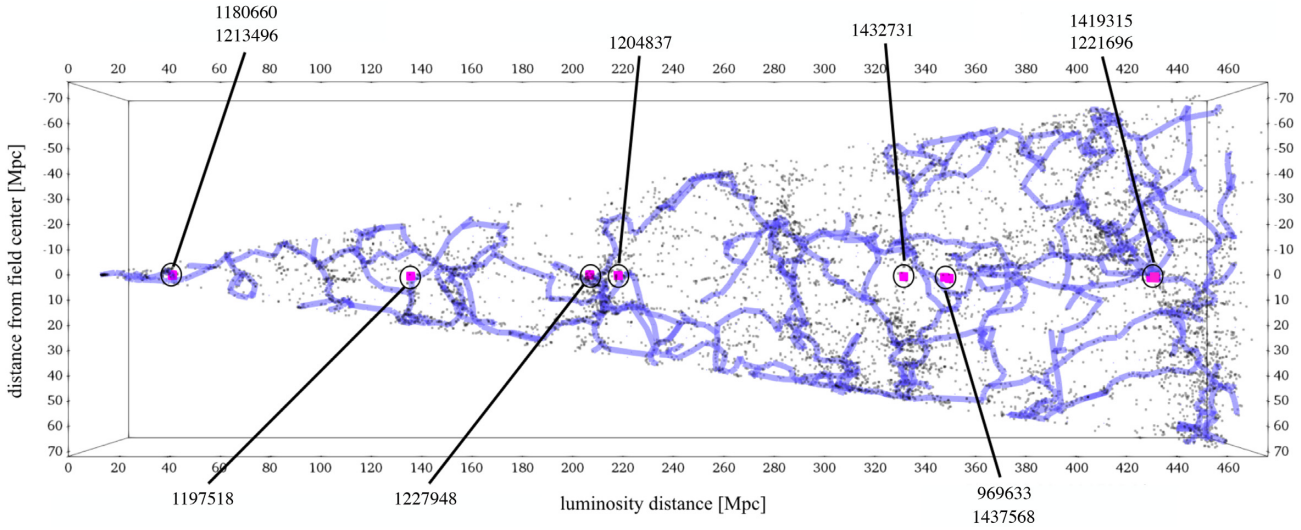

Figure 1. Filamentary network of the cosmic web, based on the DisPeSE topological algorithm, overlaid on the distribution of galaxies in the redshift range $0 < z < 0.1$. The black squares represent SDSS-DR14 galaxies with known optical spectroscopic redshifts and the pink squares show the galaxies in the H I sample. At the edges of the figure, the filaments are mostly parallel to the edge of the sample. This is an artefact of the filament detection, due to galaxy density rapidly dropping at the survey edges. Note that the CHILES field of view is a slim cone with an extent of 5 Mpc at $z = 0.1$.

Table 3. Galaxy properties of the sample.

Galaxy ID (1)	COSMOS 08 ID (2)	RA (J2000) (3)	Dec. (J2000) (4)	H I (Optical) Redshift (5)	Dist. (Mpc) (6)	V_{sys} (km s^{-1}) (7)	Type (8)	Dist. near (Mpc) (9)	Dist. fil (Mpc) (10)	Fig. (11)
J100128.00+022025.4	1213496	150.3666	2.3403	0.0068 (0.0069)	30	2041	dIrr	0.173	0.295 ± 0.089	A1
J100153.77+022449.8	1180660	150.4741	2.4139	0.0068 (0.0068)	30	2046	dIrr	0.173	0.319 ± 0.062	A2
J100115.19+021824.4	1197518	150.3130	2.3068	0.0286 (0.0266)	130	8575	Irr	1.5	3.7 ± 0.1	A3
J100055.21+022343.8	1204837	150.2300	2.3955	0.0445 (0.0446)	205	13335	Sp	0.371	3.4 ± 0.3	A4
J100041.07+022446.7	1227948	150.1711	2.4130	0.0470 (0.0425)	217	14113	Irr	0.371	3.6 ± 0.3	A5
J100103.70+023053.1	1432731	150.2654	2.5148	0.0718 (0.0714)	337	21554	Sp	1.2	9.6 ± 0.2	A6
J100115.50+022858.5	1437568	150.3145	2.4829	0.0753 (0.0752)	354	22596	bSp	1.7	7.1 ± 3.5	A7
J100130.00+021705.0	969633	150.3748	2.2848	0.0756 (0.0750)	356	22676	bSp	1.7	6.0 ± 3.4	A8
J100109.33+022823.8	1419315	150.2889	2.4732	0.0930 (0.0927)	443	27896	Sp	0.265	5.5 ± 0.5	A9
J100116.64+022704.0	1221696	150.3194	2.4511	0.0927 (0.0927)	441	27802	Irr	0.265	5.7 ± 0.4	A10

Notes. (1) Galaxy ID; (2) COSMOS 08 ID; (3) units of right ascension are in degrees; (4) units of declination are in degrees; (5) H I redshift is from CHILES and optical redshifts are from the G10/COSMOS v05 catalogue; (6) distance to target galaxy; (7) system velocity; (8) galaxy morphological classification, done by eye; (9) distance to nearest neighbour; (10) distance to nearest filament; (11) figure in the Appendix.

Table 4. Stellar and H I properties of the sample.

COSMOS 08 ID (1)	rms (μJy bm^{-1}) (2)	Beam (arcsec^2) (3)	Abs. mag. (W) (4)	NUV − r (5)	SFR ($M_\odot$ yr^{-1}) (6)	M_* 10^9 ($M_\odot$) (7)	$M_{H\,I}$ 10^9 ($M_\odot$) (8)	$M_{H\,I}/M_*$ (9)	D_{Opt} (kpc) (10)	$D_{H\,I}$ (kpc) (11)
1213496	76	6.42 × 4.74	−14.0	1.8	0.002	0.0006	0.018 ± 0.006	30.7	1.3	1.4
1180660	76	6.42 × 4.74	−15.1	1.4	0.02	0.02	0.029 ± 0.005	1.3	3.0	2.3
1197518	74	6.49 × 4.83	–	1.8	0.05	0.4	1.7 ± 0.2	4.2	13	22
1204837	79	6.60 × 4.93	−21.6	4.3	0.2	13.3	4.2 ± 1.4	0.3	27	30
1227948	79	6.60 × 4.93	–	1.8	0.03	0.2	0.9 ± 0.3	5.3	7.3	19
1432731	86	6.77 × 5.08	−19.7	1.0	0.6	8.2	11.2 ± 3.1	1.4	10	63
1437568	86	6.77 × 5.08	−20.8	3.0	1.9	14.8	5.2 ± 3.0	0.4	23	39
969633	86	6.77 × 5.08	−21.2	2.6	1.6	11.5	9.6 ± 2.9	0.8	25	47
1419315	83	6.80 × 5.10	−20.7	2.4	2.4	7.6	6.3 ± 3.8	0.8	26	34
1221696	83	6.80 × 5.10	−19.5	1.3	0.9	2.5	3.2 ± 2.5	1.3	16	12

Notes. (1) COSMOS 08 ID; (2) mean rms of the image cube; (3) synthesized beam FWHM of the image cube; (4) SDSS z-band absolute magnitude; (5) NUV − r, using *GALEX* NUV magnitude and SDSS-DR7 r-band magnitude; (6) SFR; (7) stellar mass; (8) H I mass, corrected for the primary beam; (9) gas fraction; (10) optical diameter along the SDSS r-band isophotal major axis; (11) H I diameter along the H I major axis, corrected for the beamwidth.

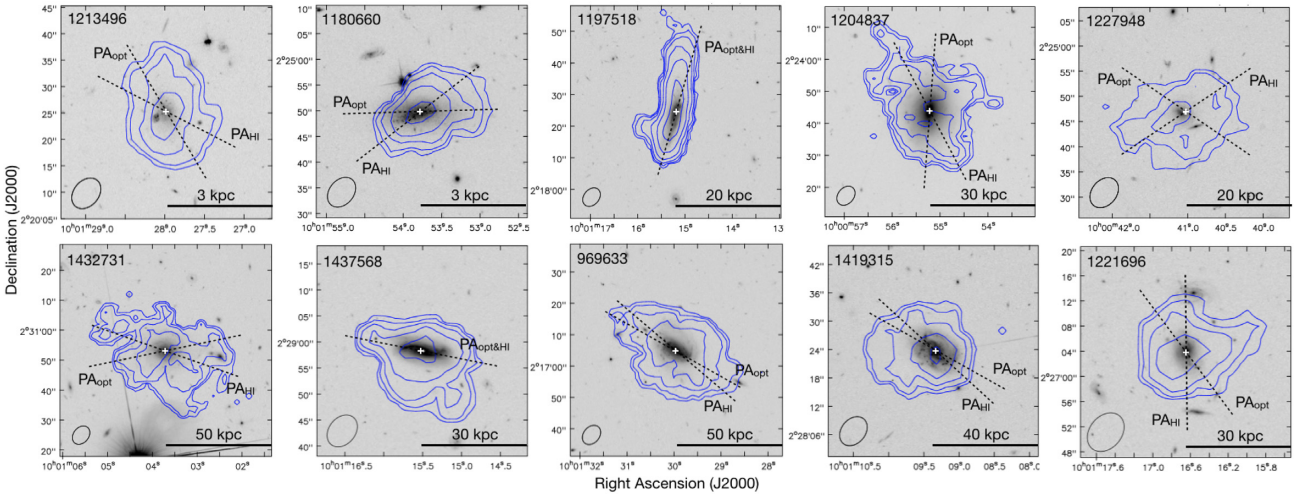

Figure 2. Total H I intensity maps of the sample. The total integrated flux contours are 2, 4, 8, 16, and 32σ. The contour values in cm^{-2} are listed in the Appendix (Figs A1–A10) for each galaxy.

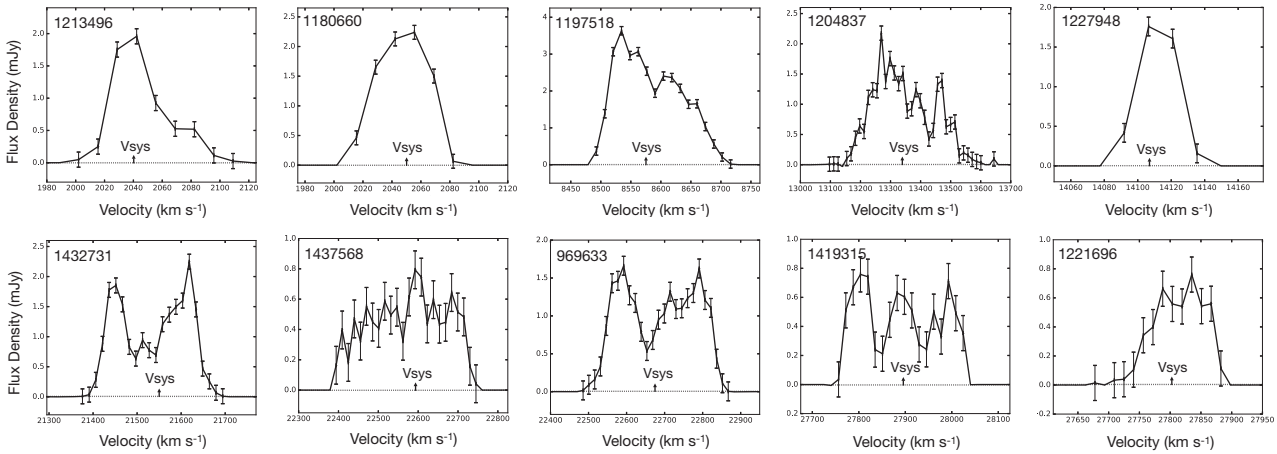

Figure 3. Global H I profiles for the sample. The H I system velocity is indicated with an upward-pointing arrow on the profile.

Table 5. Stellar, H I, and H α properties of the sample.

COSMOS 08 ID (1)	Incl. (deg) (2)	W_{int} (km s^{-1}) (3)	W_{20} (km s^{-1}) (4)	W_{pvd} (km s^{-1}) (5)	$W_{H\,\alpha}$ (km s^{-1}) (6)	PA$_{opt}$ (deg) (7)	PA$_{H\,\alpha}$ (deg) (8)	PA$_{H\,I}$ (deg) (9)	PA offset (deg) (10)	Spin$_*$ Diff (deg) (11)	Spin$_{H\,I}$ Diff (deg) (12)
1213496	39	120	69	55	NA	30	NA	242	32	0	32
1180660	65	80	63	80	80	91	84	127	36	61	83
1197518	72	244	180	190	160	165	163	163	2	3	5
1204837	43	509	323	355	135	−5	175	207	32	42	10
1227948	40	69	42	45	40	55	54	303	68	18	86
1432731	14	324	222	240	240	101	101	70	31	21	10
1437568	61	353	311	350	300	78	258	258	0	54	54
969633	25	395	287	350	280	60	240	229	11	72	83
1419315	49	300	248	265	230	60	240	227	13	19	6
1221696	49	215	125	150	120	36	180	180	36	5	41

Notes. (1) COSMOS 08 ID; (2) inclination is calculated such that 0° is face-on; (3) H I line width over which the global H I profile is integrated; (4) H I line width measured at 20 per cent of the peak flux density; (5) H I line width measured at the maximum velocity of the rising and declining parts of the H I PV diagram; (6) H α line width measured at the maximum velocity of the rising and declining parts of the H α rotation curve; (7) Optical PA; (8) H α PA; (9) H I PA; (10) difference between the optical and H I PAs; (11) difference between the stellar spin angle and filament angle; (12) difference between the H I spin angle and filament angle.

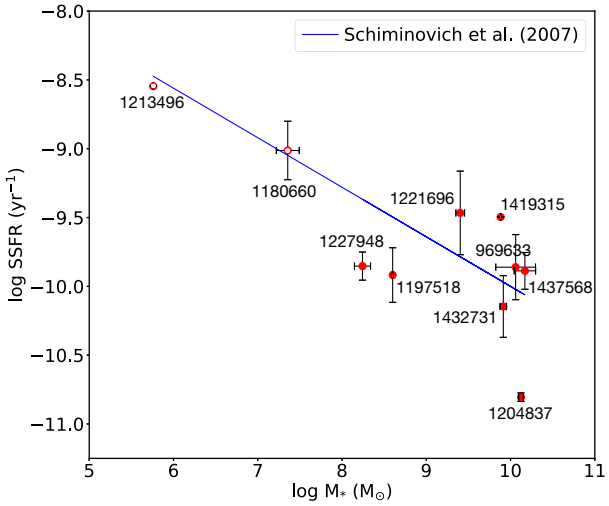

Figure 4. Relation of the SSFR and stellar mass. The blue line shows the fit to the star-forming sequence for an SDSS spectroscopic sample of galaxies using *GALEX* ultraviolet luminosities to measure the SFR in Schiminovich et al. (2007). Open symbols are small galaxies with uncertain stellar masses.

galaxies and active bulge-dominated galaxies. The one outlier in our sample, 1204837, appears to lie in this green valley. In the *HST* image, this galaxy appears to be a bulge-dominated system, which has a high stellar mass, a lower SFR, and an NUV − r of 4.3.

3.2 H I data analysis

Sub-cubes with individual galaxies, described in Section 2.1, are used to produce total H I intensity maps (zeroth moment) and velocity fields (first moment) using SoFiA, the Source Finding Application (Serra et al. 2015). A noise scaling filter is applied along the velocity axis to normalize the cube by the local noise level per channel to account for variable noise characteristics throughout the cube. The S&C algorithm (Serra, Jurek & Flöer 2012) is used to search for emission at multiple resolutions by smoothing the cube in three dimensions with specified kernels. The cube is smoothed at two resolutions in the sky using Gaussian kernels. The kernels are 4 × 4 and 6 × 6 pixels, which equal roughly 1.5 and two times the synthesized beam, respectively. The cube is smoothed at multiple resolutions in velocity using boxcar kernels. The kernels vary from 3 to 11 times the channel width, with the combination depending on the width of the spectrum of the galaxy. At each resolution, a specified relative flux threshold (in multiples of the noise level) is applied to extract and mark the significant pixels on each scale. The threshold varies from 3.5 to 4 for moment 0 maps. Higher threshold ranges of 4–6 are used for moment 1 maps, as they are more sensitive to the noise. A final mask is produced through the union of the masks constructed at the various resolutions, with significant pixels merged into this final source mask that is then applied to the input cube.

We present figures for individual galaxies in the Appendix (Figs A1–A10). The total H I intensity or moment 0 maps of each galaxy are overlaid as contours on *Hubble Space Telescope* (*HST*) Advanced Camera for Surveys (ACS) *I*-band (F814W) mosaic images (Figs 2, 13, and A1–A10) obtained from the COSMOS Archive and IRSA cut-out service (Koekemoer et al. 2007; Massey et al. 2010). The optical centre is marked with a white cross. The H I major axis is shown as a dotted line with the PA of the receding side. The optical major axis is also shown as a dotted line. The H I intensity-weighted velocity fields or moment 1 maps are similarly overlaid as contours on *HST* images. On the velocity field, the line passing through the cross represents the H I system velocity, $V_{\rm H\,I}$. All nearby background galaxies with known redshifts in the *HST* images are confirmed to be distant enough to be ruled out of association or interaction with our targets. Only one target (1221696) has a neighbouring galaxy's emission detected in the SALT spectra, but it is >30 000 km s^{-1} in separation.

The 2D position–velocity (PV) slices are extracted along the H I major (ϕ) axis and minor ($\phi + 90$) axis. The optical centre and the H I PA, shown in the upper-left corner, are used to make slices. The optical centre of the slice and the H I system velocity are indicated with dashed lines. The global H I profiles for the sample (Figs 3 and A1–A10) are produced by summing the flux in each channel using the source masks produced by SoFiA. Details on determining the H I system velocity and the PA for the H I major axis are found in Section 3.4. The contour levels of the H I emission in the PV diagrams, the H I column density in the total H I intensity maps, and the H I velocities of the H I intensity-weighted velocity fields are listed in the captions of Figs A1–A10 in the Appendix.

3.3 H α data analysis

The ionized gas rotation curves are constructed using PYTHON curve-fitting routines to fit single Gaussians to the emission-line features in the 2D SALT spectra. A Gaussian is fit to each pixel row in the region of the emission line, sampling the spatial extent of the galaxy image on the CCD until the signal became too low to fit. From the optimized curve fit, a continuum fit, amplitude, wavelength centre, and full width at half-maximum (FWHM) is obtained. We use the wavelength centres to calculate a velocity. The spatial centres are assigned by finding the mid-point row of the emission profile. We note that by sampling the velocity centres at each pixel row, we are oversampling with respect to the seeing (0.25 arcsec versus ∼1 arcsec), but even when averaged, the rotation curve shape remains intact. Additionally, we note that while single Gaussians fit most of the emission-line data well, two galaxies (1197 518 and 1419 315) exhibited profiles that are not well fit by a single Gaussian. Details on the fitting of these two galaxies can be found in the sample descriptions in Section 3.6.

For seven of the galaxies in the sample, the optical SALT spectra exhibited one or both lines of the doublets [N II] λλ6548, 6583 and [S II] λλ6716, 6732. Though not necessary for the kinematic analysis, we use these emission lines to derive line ratios across the slit region of each galaxy to search for any potentially interesting features in the ionized gas. The [N II] and [S II] lines are fit with the same method as described for H α. The optimal continuum fit is then subtracted before calculating the area under the fit for H α, [N II], and [S II]. The ratios [N II]λ6583/H α and [S II]λ (6716 + 6732)/H α are then calculated row by row, sampling the ratio across the galaxy. One-sigma errors are derived from the Gaussian fits and propagated. Due to heavy residuals from the subtraction of night skylines, it is not always possible to fit one or both of the [S II] doublet lines. Given that the [S II] doublet lines are often comparable in intensity, for the galaxy in which we could not fit both lines, we make a very rough approximation of simply doubling the value derived from the fitted line.

The median of the line ratios across each disc is compared to Sloan Digital Sky Survey (SDSS) values and found to be in decent agreement for all targets for which SDSS data are available, as shown in Table 6. All but three galaxies in our sample exhibited

Table 6. Line ratio summary.

C08 ID	N II/H α Obs[a]	S II/H α Obs	N II/H α SDSS[b]	S II/H α SDSS	O III/H β SDSS
1197518	0.07 ± 0.02	–	–	–	–
1204837	0.43 ± 1.20	–	0.85	0.95	1.30
1432731	0.28 ± 0.03	0.29 ± 0.03	0.31	0.35	0.30
1437568	0.40 ± 0.01	0.33 ± 0.03	0.41	0.37	0.43
969633	0.51 ± 0.12	0.34 ± 0.12	0.60	0.26	0.36
1419315	0.33 ± 0.06	–	–	–	–
1221696	0.15 ± 0.03	0.51 ± 0.09	–	–	–

Notes. [a]Median value of all fit points across target; [b]values for 3 arcsec diameter fibre centred on target.

some or all of these forbidden lines, representing galaxies with SFRs between 0.05 and 2.4 $M_\odot$ yr^{-1}. While the median line ratio values for these galaxies agree with SDSS values, we find that there is some variation in the values across the discs. The [N II] emission in 1204 837, the galaxy with the lowest SFR of the galaxies with detectable [N II] emission is too weak for spatially resolved study, but for the other six galaxies, we are able to trace the line ratio across the inner disc (Fig. 5). Only the innermost disc (out to radii of 3–6 arcsec) is measured (see plots in Figs A1–A10 for galaxy images). None of the galaxies for which there are SDSS O[III] data are beyond the star-forming region of a Baldwin–Phillips–Terlevich (BPT) diagram (Baldwin, Phillips & Terlevich 1981). As a final probe, we apply the simple metallicity scaling relationship developed by Dopita et al. (2016) across the disc (Fig. 5). This relationship uses a ratio of [N II]/[S II] and [N II]/H α to obtain a 12 + log(O/H) metallicity value without the use of oxygen lines, which suffer from reddening effects or go unobserved without multiple spectrograph configurations. For the galaxies that contained the necessary nitrogen and sulphur lines, we find that, like the [N II]/H α ratio, the metallicity peaks in the centre and decreases with increasing radius in the disc, as expected from typically negative radial metallicity gradients found in the discs of late type galaxies (Marino et al. 2013; Belfiore et al. 2017). The line ratio properties of each target are discussed in Section 3.6.

3.4 H I and H α properties

H I properties for the galaxies are listed in Tables 3 and 4. The H I mass is calculated as

$$M_{\rm H\,I} = 49.8\, d^2 \int s(\nu) {\rm d}\nu \ [{\rm M}_\odot], \tag{2}$$

where d is the luminosity distance in Mpc, s is the flux density in Jy, ν is the frequency in Hz, and flux is the integral of $s{\rm d}\nu$ in Jy Hz. The integrated flux is determined as the sum of all flux density values within the source mask generated by SoFiA. This value is multiplied by the spectral channel width and divided by the number of pixels per beam to get flux in units of Jy Hz. The 5σ H I mass sensitivity of our observations over 150 km s^{-1} is 1.9×10^7 $M_\odot$ at $z = 0.0068$ and 3.5×10^9 $M_\odot$ at $z = 0.0930$. Our sample galaxies have H I masses ranging from 1.8×10^7 (velocity width 120 km s^{-1}) to 1.1×10^{10} $M_\odot$, with six galaxies between 10^9 and 10^{10} $M_\odot$ and one galaxy above $10^{10} M_\odot$. The H I masses have been corrected for the primary beam. Throughout the H I cubes, we used the areas outside of the H I emission to measure the rms. We estimate the H I mass to have an uncertainty on the order of 20 per cent.

The column densities for individual galaxies are given in the captions of Figs 2 and A1–A10 in the Appendix. The H I column density is calculated as

$$N_{\rm H\,I} = \frac{2.34 \times 10^{20}}{\theta_1 \theta_2} (1+z)^4 \int s(\nu) {\rm d}\nu ({\rm cm}^{-2}), \tag{3}$$

where θ_1 and θ_2 are the FWHM of the major and minor axes of the synthesized beam in arcsec, z is the redshift, s is the flux density in Jy, ν is frequency in Hz, and flux is the integral of $s{\rm d}\nu$ in Jy Hz. We reach the theoretical noise in our image cubes and reach the predicted column density level of 3×10^{19} cm^{-2} (13 km s^{-1} channel at $z \sim 0$).

Additional H I properties listed in Tables 3 and 4 are the system velocity, the line width of the galaxy, the radial extent of the H I, and the PA of the H I. $V_{\rm sys}$ is taken as the velocity value at the optical centre of the velocity field. $W_{\rm int}$ is the line width over which the global H I profile is integrated and is taken from the channel range of the source mask used to generate moment 0 images in SoFiA. W_{20} is the line width measured at 20 per cent of the peak flux density. $W_{\rm pvd}$ is the line width measured at the maximum velocity of the rising and declining parts of the H I PV diagram. Similarly, $W_{\rm H\,\alpha}$ is the line width measured at the maximum velocity of the rising and declining parts of the H α rotation curve. Errors of 27 km s^{-1} in the H I line widths reflect uncertainties of one channel on either side.

The radial extent of the H I diameter $D_{\rm H\,I}$ is measured along the H I major axis of the P–V diagram at a limiting column density of 1.25×10^{20} cm^{-2} (1 $M_\odot$ pc^{-2}). $D_{\rm H\,i}$ is corrected for beam smearing effects using a Gaussian approximation (Wang et al. 2016):

$$D_{\rm H\,I} = \sqrt{(D^2_{\rm H\,Io}) - (B^2)}, \tag{4}$$

where $D_{\rm H\,I}$ and $D_{\rm H\,Io}$ are the corrected and uncorrected H I diameters, and B is the synthesized beam along the major axis. Errors of 11 arcsec in the H I radial extent reflect uncertainties of one beamwidth on either side.

$\rm PA_{H\,I}$ is calculated using SoFiA to determine the flux-weighted centroid of the emission in each channel of the image cube and then fitting a straight line to the set of centroids. Errors of 10° in the H I PA reflect an uncertainty estimate of 5° on either side. The PA is compared by eye to the H I kinematic major axis of the velocity field. The PA is adjusted to match the H I kinematic major axis of the velocity field in 1432731 and 1221696. $\rm PA_{H\,\alpha}$ is taken at the optical major axis or close to it, as described in Section 2.2.

3.5 Identifying galaxy environments

To quantify the environments of galaxies, we look at their location in the cosmic web and the distance to the nearest neighbour. Luber et al. (2019) has developed the use of DisPerSE for the CHILES volume using a catalogue of 11 500 spectroscopic redshifts from the G10/COSMOS v04 catalogue (Davies et al. 2015). They show that for this small volume sensible results are obtained that are consistent with larger surveys. Here, we use the same method, but we use redshifts from SDSS-DR14 rather than from G10/COSMOS v04 since too few redshifts are available at this low redshift in G10/COSMOS v04. We search SDSS-DR14 for all galaxies with spectroscopic redshifts with coordinates 148° < RA < 153°, and 0° < Dec. < 5° which corresponds to a thickness of 70 Mpc at the higher end of the redshift range and 15 Mpc at the lower end of the redshift range. We choose an area that is sufficiently wider than the actual CHILES field, to properly reconstruct the large-scale structure in the CHILES field.

We run DisPerSE over this galaxy catalogue with a mirror boundary condition and a significance level of four. See Luber et al.

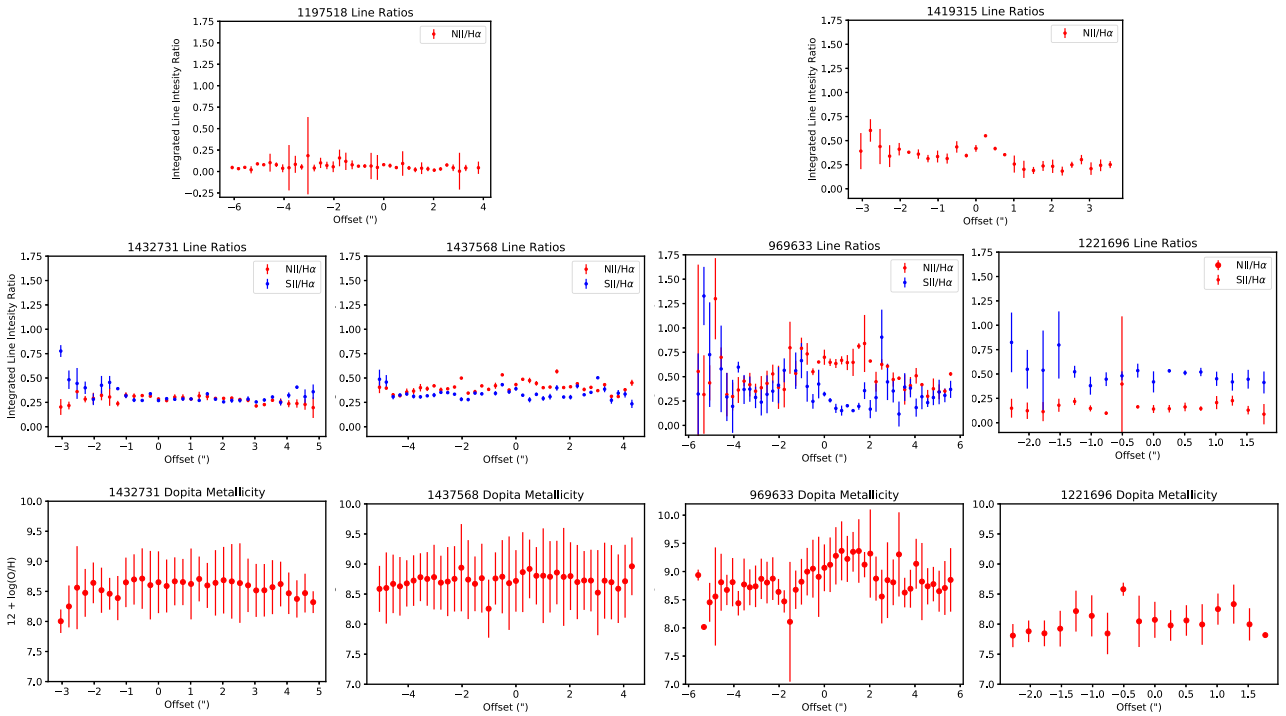

Figure 5. Top and middle row: Line ratios of [N II]λ6583/H α (red) and [S II]λ (6716 + 6732)/H α (blue) as a function of offset from the galaxy centre for all galaxies in which these emission lines are measurable. Bottom row: Metallicity across the disc of the galaxy using the relationship from Dopita et al. (2016).

(2019, section 4) for further explanation of the method and these experimentally determined parameters. DisPerSE identifies various types of structures in a density field of points by characterizing topological features that correlate to indexed manifolds that then correspond to various components of the cosmic web (voids, walls, filaments, and clusters). We extract the filament spines, with the tracers of this filamentary structure referred to as critical points. We calculate the distance of a galaxy to its nearest filament spine by finding the distance of that galaxy from the nearest critical point. The error in distance is bound by half the distance between the critical point used and the next closest one. Fig. 1 shows the 3D slice of our field of view collapsed into a 2D projection. The position of galaxies in relation to the filamentary structure is also shown in Fig. 1 and discussed in Section 5. Note that contrary to some other work where 2D distances are used (Kleiner et al. 2017; Laigle et al. 2018; Luber et al. 2019), we use 3D distances in our analysis.

The distance to the nearest neighbour is calculated by assuming all velocities are purely due to expansion, converting RA, Dec., and redshift to physical units, and finding which galaxy is the minimum distance in physical units. It is important to note that this is done with the spectroscopic catalogue as photometric redshifts are not accurate enough for low z.

3.6 Notes on individual galaxies

1213496 and 1180660: The two nearest galaxies in our sample are dwarf irregulars (Fig. A1 and A2). They are close spatially with a separation of around 70 kpc, as shown in Fig. 6(a), and have a velocity difference of 5 km s^{-1}. Both 1213496 and 1180660 lie within ∼300 kpc of filamentary structure. These galaxies have H I masses on the order of 10^7 M$_\odot$ and have the highest SSFR of our sample. Both galaxies have H I offset from the optical major axis as well as asymmetric H I morphology. In each galaxy, the optical PA follows the outer H I intensity contours while the H I PA follows the velocity field of the inner disc. For 1213496, the northern part of the velocity field in the outer disc seems to shift more towards polar. For 1180660, the velocity field looks even more disturbed with the contours to the west nearly perpendicular to the H I major axis, more like a polar ring of counter-rotating gas. Given their proximity, the disturbances in the outer discs may be an indication that these two galaxies are gravitationally interacting.

Ionized gas is not detected in 1213496 and is limited in extent in 1180660, consistent with their low SFRs. When viewing 1180660's ionized gas rotation overlaid on its H I PV diagram, we see that the ionized gas is well-aligned along with the system velocity for PA 84°, and fits well within the H I contours for PA 137°, though with a slightly steeper slope.

1419315 and 1221696: The two farthest galaxies in our sample are close spatially with a separation of around 170 kpc, and have a velocity difference of 94 km s^{-1}. 1221696 (Figs A10 and 6b) has a tail that extends in the direction of 1419315 (Fig. A9). This feature along with their proximity may indicate that they are gravitationally interacting. Both 1419315 and 1221696 are located ∼5.6 Mpc from filamentary structure. These galaxies have H I and stellar mass on the order of 10^9 M$_\odot$ and have SFRs that are some of the highest in our sample. Both have asymmetric H I morphology.

The ionized gas rotation curves in both of these galaxies mostly agree with the H I PV diagram contours. However, in 1419315, the ionized gas rotation seems to flatten/decline at a lower velocity than the H I towards the receding edge of the galaxy. The H I and H α are decoupled at large radii, which is a unique phenomenon in this sample. Galaxy 1419315 did not have measurable [S II], but did demonstrate enhanced [N II]/H α ratio at the centre, and asymmetric values (high on the approaching side and low on the receding side). This is consistent with a negative radial metallicity gradient. In galaxy 1221696, we again see little variation in the

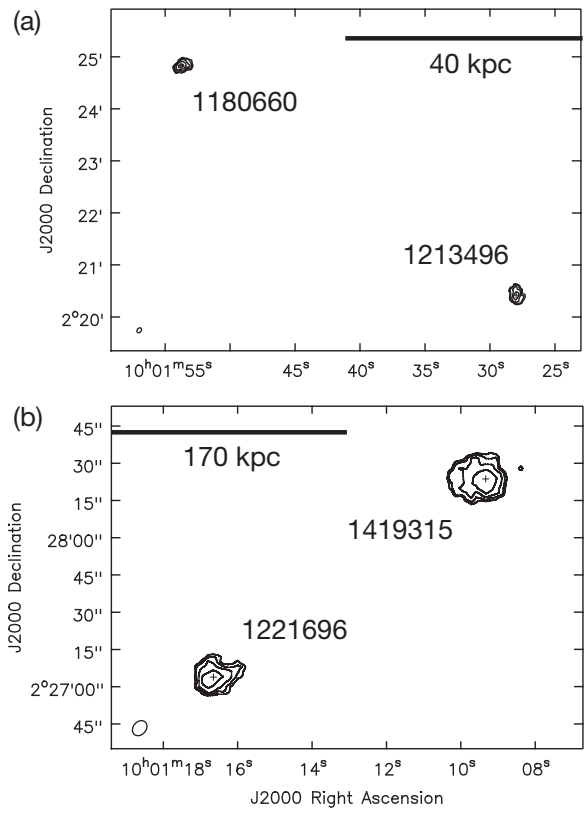

Figure 6. Galaxies in close proximity. Fig. 6(a) shows total H I intensity maps for the two nearest galaxies in our sample. They are close spatially with a separation of around 70 kpc and have a velocity difference of 5 km s^{-1}. For both galaxies, the H I velocity field of the outer disc shifts more towards being perpendicular to the H I major axis, indicative a polar ring. Their disturbed H I morphology and kinematics along with their proximity may indicate they are gravitationally interacting (Figs A1 and A2). Fig. 6(b) shows total H I intensity maps for the two farthest galaxies in our sample. They are close spatially with a separation of around 170 kpc and have a velocity difference of 94 km s^{-1}. 1221696 has a tail that extends in the direction of 1419315. This H I feature along with their proximity may indicate they are gravitationally interacting (Figs A9 and A10).

line ratios across the measured region of the disc. The [S II]/H α ratio is, however, higher at all points across the measured area of the disc. Given the limited region probed, it is difficult to draw any conclusions about these line ratio values.

1204837 and 1227948: 1204837 (Fig. A4) and 1227948 (Fig. A5) are two galaxies that are within 371 kpc of their nearest neighbour. Both galaxies have extended H I with asymmetric morphology and are located ∼3.5 Mpc from filamentary structure. Both have H I offset from the optical major axis, with irregular galaxy 1227948 having a PA offset of 68°.

The ionized gas rotation fits well with the H I PV diagram of 1204837, with both neutral and ionized gas missing from the centre of the galaxy. 1204837 has the most dominant bulge in our sample, which may account for the lack of neutral and ionized gas in the centre of the PV diagrams. 1204837 has very weak [N II] 6583 Å emission. In 1227948, the ionized gas lays along with the system velocity for both position angles, agreeing well with the H I contours (albeit with some scatter since the galaxy is irregular and one of the smallest in the sample).

1432731: 1432731 (Fig. A6) is a spiral galaxy and is the most face-on galaxy of our sample, inclined at 14°. It is at a distance of 1.2 Mpc from its nearest neighbour. This galaxy has the largest H I mass in the sample at 1.1×10^{10} $M_\odot$ and resides 9.6 Mpc from a filament spine. 1432731 has an H I diameter that is 71 kpc across, extending over six times past the optical diameter. The H I distribution and morphology are very asymmetric and the PV diagram shows lower velocity low-level emission on the receding side that could indicate counter rotation.

The ionized gas overall consistently traces the H I contours. There is a region of ionized gas emission on the receding edge, likely corresponding to a bright H II region in one of the faint extended spiral arms visible in the *HST* image of the galaxy. In 1432731, both [N II]/H α and [S II]/H α are similar values in the central region of the disc, but [N II] emission diminishes while [S II] emission increases at increasing radii. The decreased [N II] emission is consistent with decreasing metallicity. Though [S II]/H α may also trace metallicity, it does so much less reliably. When the [S II]/H α ratio is unusually high (>0.4), it can be attributed to supernova remnants (SNRs) or diffuse ionized gas (Zhang et al. 2017). Our line widths do not seem wide enough for SNRs, so the enhanced [S II]/H α at the edges of the measurable region may therefore be attributable to diffuse ionized gas. Given that the 'flared' [S II]/H α occurs around the point where the slit traverses inter-arm regions rather than spiral arms on both sides of the galaxy, this seems plausible.

1197518: 1197518 (Fig. A3) is an irregular galaxy and one of the more isolated galaxies in our sample, at a distance of 1.5 Mpc from its nearest neighbour and 3.7 Mpc from a filament spine. It is the brightest H I detection so far in the full survey and has extended H I with very asymmetric morphology. The H I mass is several times its stellar mass and the SFR is low at 0.05 $M_\odot$ yr^{-1}.

The ionized gas kinematics for this galaxy are the most irregular in the sample. Weak [N II] 6583 Å is present along with H α. Though it fits within the H I contours, the rotation curve exhibits a central kink. In the outer regions of the galaxy (−10 to −7.5 arcsec and +2.5 to +10 arcsec), the emission-line profiles are well fit by a single Gaussian. The central region is highly asymmetric, suggesting at least two components, with the dominant component shifting from red to blue as one moves from bottom to top of the galaxy spatially.

The steep rise and fall of the ionized gas in the central region may be indicative of a strong bar, though the galaxy seems to be viewed almost edge-on, making this conclusion difficult to confirm. Sofue et al. (1999) identified that, while barred galaxies exhibit similar general properties compared to unbarred galaxies, they have larger velocity amplitude variation in the innermost disc. This large velocity variation arises from the barred potential, and simulations of PV diagrams for edge-on barred galaxies show many tens of km s^{-1} fluctuations, superposed on the usual flat rotation curve (Athanassoula & Bureau 1999).

Considering this is a highly inclined galaxy, the PV diagram can also be interpreted as to have a steeply rising rotation curve at the approaching side, and a more slowly rising rotation curve at the receding side, not inconsistent with the H α. The optical morphology of the outer disc in the *HST* image of the galaxy seems suggestive of a warp. The H I contours have a mild curvature, but the ionized gas is more dramatically perturbed. With a nearest neighbour 1.5 Mpc away, a merging event seems unlikely but cannot be conclusively ruled out and lends a possible explanation for the disturbed kinematics of the ionized gas.

1437568 and 969633: Two barred spirals are the most isolated galaxies in our sample, at a distance of 1.7 Mpc from their nearest neighbour. Both 1437568 (Fig. A7) and 969633 (Fig. A8) are

located several Mpc from filamentary structure at 7.1 and 6.0 Mpc, respectively. These galaxies are large in stellar mass and have higher SFRs. Both galaxies have extended H I and 1437568 has asymmetric H I morphology.

The ionized gas emission in 969633 extends to 8 arcsec along PA = 60°, corresponding to a distance of 19.9 kpc, or ∼ 80 per cent of the stellar radius ($R_* = 24.44$ kpc). The profile of this galaxy differs from the rest of the sample due to the presence of a very broad, bright central region. The outer disc is fit by relatively narrow (FWHM < 1 Å) Gaussians, but the central region has characteristic widths of 3 Å or 120 km s^{-1}. The galaxy is not, however, an AGN. Line ratios measured using H α, [N II], and [S II] from the SALT spectrum, as well as SDSS spectrum values for [O III]λ5007/H β, place this galaxy firmly within the star-forming region of a BPT diagram (Baldwin et al. 1981). We thus attribute the broad-line widths in the central region to the kinematic influence of the bar (see Section 3.3). The ionized gas matches the H I spatially and kinematically. The ionized gas rotation can be traced through the central region, where no H I is detected for the chosen position angle. The ionized gas in 1437568 is mostly unremarkable, following the H I contours in slope and velocity centre.

In galaxy 1437568, the line ratios remain relatively flat across the measured portion of the disc, albeit with more scatter than other galaxies in the sample. Though it is a barred spiral, we do not see a significant enhancement of [N II]/H α (see 969633 notes). The most interesting of the sample in terms of line ratios is 969633, with enhanced [N II]/H α and suppressed [S II]/H α in the central region. Given that this galaxy has the broadest line widths in the centre in H α, it would seem there is intense activity in the innermost part of the disc, though it does not qualify as an AGN. The enhanced [N II]/H α likely arises from the bar in 969633. Florido et al. (2015) find that barred galaxies exhibit an enhanced N/O ratio, and thus higher [N II]/H α. They find no similar effect on [S II]/H α in agreement with the [S II]/H α values remaining mostly flat across the region of enhanced [N II]/H α.

4 SCALING RELATIONS

We analyse ancillary stellar data along with the observed H I and H α properties of our sample and find our data follow known galaxy scaling relations. Our sample follows expected trends for star formation rates, H I gas fraction, and the H I size–mass relation as well as the baryonic Tully–Fisher relation for the H I and H α.

4.1 H I gas fraction

The relation between M_* and $M_{\rm H\,I}$ for our sample is shown in Fig. 7. The diagonal grey solid line indicates equal amounts of stellar and H I mass. The average gas fraction ($M_{\rm H\,I}/M_*$) of our sample is 1.8 (Table 4). This is excluding 1213 496, which has a gas fraction of 31 and our highest SSFR. We compare our sample with the galaxy population detected by ALFALFA, the largest wide-field blind H I survey at low redshift (Haynes et al. 2011). The orange line shows the median values from the spectroscopic ALFALFA–SDSS galaxy sample in Maddox et al. (2015). Our sample shows $M_{\rm H\,I}$ increasing as a function of M_* and agrees quite well with the median values of the ALFALFA sample. Galaxies with stellar masses below 10^9 M$_\odot$ have more H I than stars, and galaxies with stellar masses above 10^{10} M$_\odot$ have less H I than stars. The galaxies in our sample with stellar masses below $10^{9.5}$ M$_\odot$ are all classified as irregular.

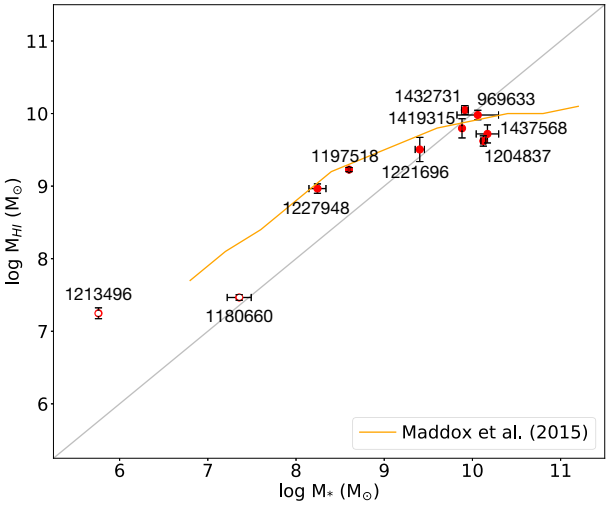

Figure 7. Relation of the H I mass and stellar mass. The diagonal grey solid line indicates equal amounts of stellar and H I mass. The orange line shows the median values from the spectroscopic ALFALFA-SDSS galaxy sample in Maddox et al. (2015). Open symbols are small galaxies with uncertain stellar masses.

4.2 H I deficiency

The H I content of galaxies can be characterized by scaling relations between the H I content and other intrinsic properties of galaxies. These H I scaling relations can be useful in identifying galaxies that have either more H I than expected or less H I than expected, as galaxies like these may have been affected by recent processes including the removal or accretion of gas. One way to characterize the H I gas content of galaxies is with H I deficiency. H I deficiency is the logarithmic difference between the observed H I mass and the expected H I mass:

$$\mathrm{H\,I_{def}} = \log M_{\mathrm{H\,I exp}} - \log M_{\mathrm{H\,I obs}}, \quad (5)$$

where $M_{\rm H\,I exp}$ is the expected H I mass calculated from scaling relations, and $M_{\rm H\,I obs}$ is the measured H I mass taken from observations (Haynes & Giovanelli 1984). Generally, a galaxy is considered to have a normal H I gas content if its H I deficiency is between −0.3 and 0.3 (Dénes, Kilborn & Koribalski 2014), with an H I excess if <−0.3 and H I deficiency if >0.3.

Studies use H I-selected samples combined with SDSS optical properties to derive scaling relations. With the GASS survey, Catinella et al. (2012) found that a good predictor of the H I content is the linear combination of stellar surface density and NUV−r colour. We examine the H I deficiency of our sample adapting results using the H I to stellar mass fraction function shown in fig. 8 from Catinella et al. (2012):

$$\log M_{\rm H\,I}/M_* = a \log \mu_* + b\,(\mathrm{NUV} - r) + c, \quad (6)$$

with $a = -0.285$, $b = -0.366$, and $c = 2.872$. This function is the relation between H I mass fraction and a linear combination of stellar mass surface density and NUV − r colour with the relation obtained using the subset galaxies with NUV − $r \leq 4.5$ mag. The stellar mass surface density is calculated from the formula

$$\mu_* = \frac{M_*}{2\,\pi\,R_{50z}^2}\ [\mathrm{M_\odot\ kpc^{-2}}], \quad (7)$$

where R_{50z} is the radius containing 50 per cent of the Petrosian flux in z-band from SDSS DR7, and NUV − r is the *GALEX* (Martin et al. 2005) NUV magnitude minus the SDSS DR7 r-band magnitude.

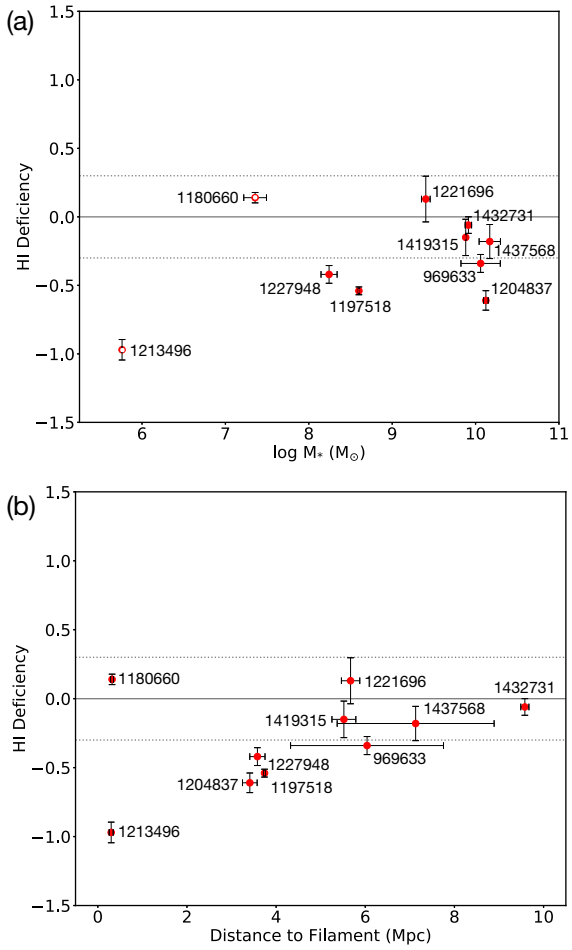

Figure 8. H I deficiency using scaling relations from Catinella et al. (2012). A solid grey line is drawn for deficiency = 0 and a dotted grey line for deficiency = +0.3 and −0.3. Fig. 8(a) shows the H I deficiency in relation to the log of stellar mass. Fig. 8(b) shows the H I deficiency in relation to the distance from filamentary structure based on the DisPeSE topological algorithm. Open symbols are small galaxies with uncertain stellar masses.

The results for H I deficiency are shown in Fig. 8. A solid grey line is drawn for deficiency = 0 and a dotted grey line for deficiency = +0.3 and −0.3. Figs 8(a) and (b) show the H I deficiency in relation to stellar mass and distance to filament, with no obvious trends. In Catinella et al. (2012), the results are for a sample of galaxies with stellar mass greater than 10^{10} $M_\odot$. Since only three galaxies (1204837, 1437568, 969633) are above stellar mass 10^{10} $M_\odot$, this method is not well calibrated for our lower mass sample. With that said, none of the galaxies are H I deficient and half of the sample has H I excess. This is of course not surprising for a small H I-selected sample.

4.3 H I size–mass relation

H I often extends beyond the optical disc, where it can trace events of removal and accretion of gas. Observationally, these events can be revealed by the asymmetries of the morphology and kinematics of H I (Sancisi et al. 2008). The majority of galaxies in our sample show extended H I. There is a tight correlation between the H I mass and the beam-corrected diameter of the H I discs, as shown in Fig. 9. The radial extent of our H I diameters $D_{\rm H\,I}$ is measured along the H I major axis of the PV diagram at a limiting column density of 1.25×10^{20} cm^{-2} (1 $M_\odot$ pc^{-2}). $D_{\rm H\,I}$ is corrected for beam smearing

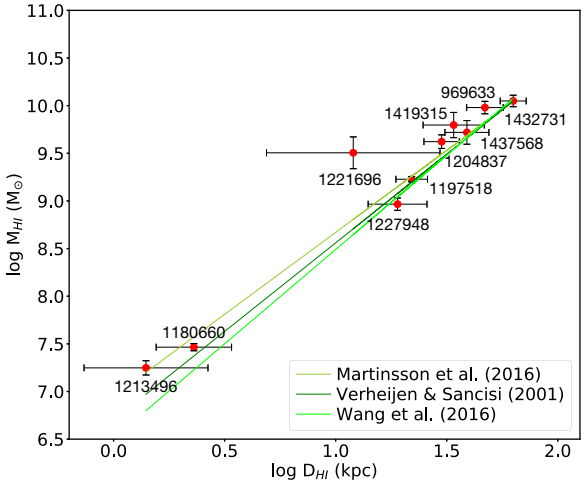

Figure 9. Relation of the H I mass and H I disc diameter. To the radial extent of the H I diameter $D_{\rm H\,I}$ is measured along the H I major axis of the PV diagrams at a limiting column density of 1.25×10^{20} cm^{-2} (1 $M_\odot$ pc^{-2}) and corrected for beam smearing. The lime green line is the correlation found by Wang et al. (2016), the dark green line represents the correlation found by Verheijen & Sancisi (2001) and the olive green line is the correlation found by Martinsson et al. (2016). Note that these papers use azimuthally averaged surface density to measure $D_{\rm H\,I}$, while we use a 1D PV diagram.

effects. The correlation of H I mass and diameter in the plot shows that as discs become more massive, they grow in size and implies a nearly constant H I surface density regardless of size.

Verheijen & Sancisi (2001) show, in their sample of 43 spirals, at least half have lopsided H I distribution and/or kinematics. Moreover, Swaters et al. (2002) examine 73 late-type dwarf galaxies and find that lopsidedness is as common among dwarf galaxies, as it is in spiral galaxies. Furthermore, Jütte et al. (2013) conduct a statistical investigation of 76 H I discs finding at least 50 per cent of galaxies have lopsided discs and that generally morphological and kinematic irregularities are correlated. Most of the galaxies in our sample have irregularities in the morphologies and kinematics of their gas discs and our results do not appear to be that unusual.

4.4 H I and H α line widths

With our sample of galaxies, we study the structural relation of H I and H α discs with rotation curves of H α in the inner regions and with H I in the outer regions. The H α traces the kinematics at a spatial resolution of 1 arcsec and a velocity resolution of 70 km s^{-1}. The H I traces the kinematics at a spatial resolution of 5 arcsec and a velocity resolution of ∼13 km s^{-1}.

A comparison of H I and H α at low redshift is useful for studies at high redshift, where only optical lines are observable. Studies at higher redshift provide information for scaling relations used in mass modelling of galaxies and in studying the evolution of the Tully–Fisher relation. We compare the line width of the H I versus the line width of the H α for our sample, as shown in Fig. 10(a). The H α PA is taken at the optical major axis or close to it, as described in Section 2.2. The H I PA is taken at the kinematic major axis, which differs from the optical major axis in more than half of the sample and may be a reason for the slight difference in widths between the H I and H α. Except 1197518 and 1204837, the line width of the H α is of the same order as the line width of the H I. This indicates that the flat part of the rotation curve is reached for H I and H α, even though the rotation curve may not completely flatten for all our galaxies in H α. Uncertainty on the H α measurements has been visualized

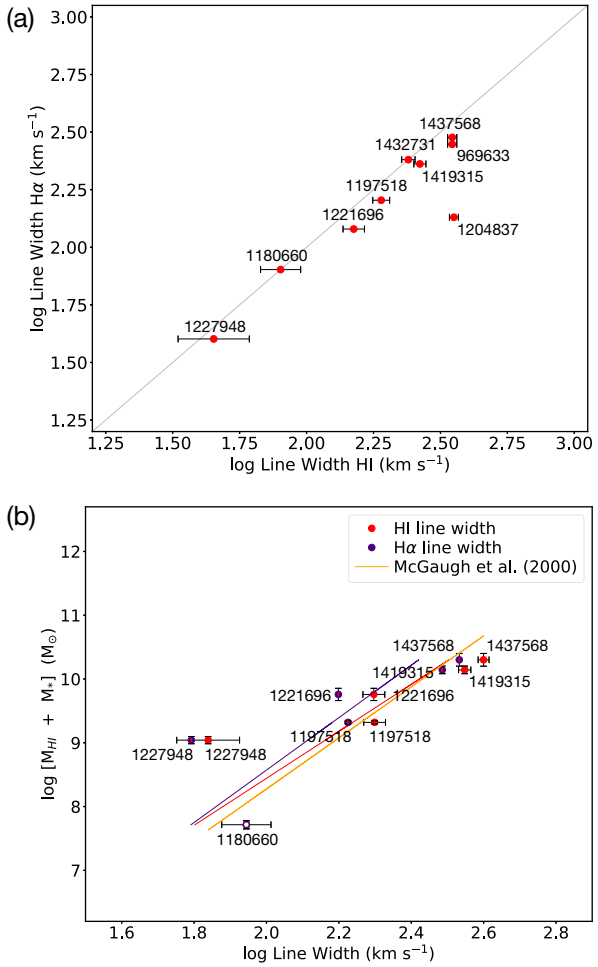

Figure 10. Line widths of the neutral and ionized gas. Fig. 10(a) shows the relation of the width of H I and the width of H α. The diagonal grey solid line indicates equal widths of H I and H α. Fig. 10(b) shows the Baryonic Tully–Fisher relation with total mass ($M_{\rm H\,I}$ + $M_{\star}$) versus the width of H I and H α. The BTFR from McGaugh et al. (2000) is shown in orange. Open symbols are small galaxies with uncertain stellar masses.

as a shaded red region on the PV diagrams (Figs A1–A10), which represents the SALT velocity resolution of ∼70 km s^{-1} for the gratings used. This uncertainty is almost certainly an overestimate, as the emission-line profiles can be fitted with much higher accuracy. However, the errors on the Gaussian velocity centres are <5 km s^{-1} for all points but the extreme edges, and thus nearly invisible when overlaid on the PV diagram.

Pisano et al. (2001) compare line widths for H I and H α and find that for larger galaxies the line widths are similar but for smaller galaxies, there is a larger spread and the H α line width is usually smaller. We find that the H I and H α line widths are generally the same, with the exception of one galaxy. For galaxy 1204837, the H α PA of the slit is not aligned with the major axis and does not trace the full velocity width.

4.5 H I and H α baryonic Tully–Fisher relation

Despite the diverse formation histories of individual galaxies, local disc galaxies exhibit a tight relationship between their rotation velocity and their luminosity or mass, namely the Tully–Fisher (TF) relation (Tully & Fisher 1977). Combining the stellar mass

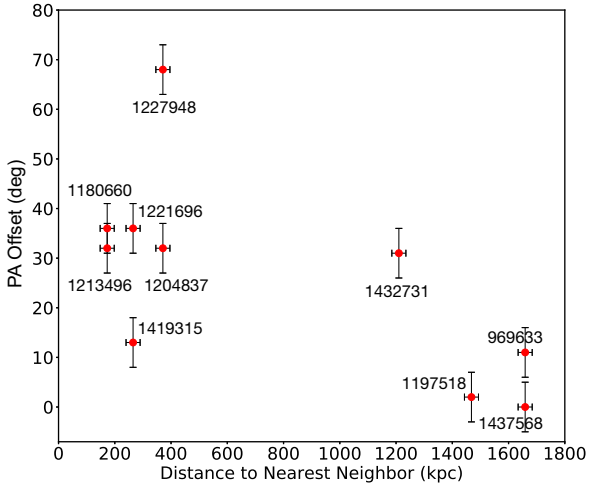

Figure 11. Relation of the PA offset and distance to nearest neighbour. PA offset is the difference between the H I kinematic major axis and the optical photometric major axis.

with observed gas mass results in a Baryonic Tully–Fisher Relation (BTFR) that is linear over many decades in mass (Verheijen 2001).

Fig. 10(b) shows BTFR for our sample, with the total mass ($M_{\rm H\,I}$ + $M_{\star}$) versus the line width of the H I and H α. Line widths used in our Tully–Fisher comparisons are corrected for inclination, with 1432731 ($i = 14°$) and 969633 ($i = 25°$) excluded from the relation. Lelli et al. (2019) study the BTFR at $z = 0$ using 153 galaxies from the SPARC sample with H I and H α rotation curves. They find the tightest BTFR is given by using the mean velocity along the flat part of the rotation curve with a best-fitting slope of 3.85 ± 0.09. The slope of the line using the H I widths from our sample is 3.68 ± 0.66 and the slope of the line using the H α widths is 4.11 ± 0.83. This is excluding 1204 837 as this galaxy is an outlier in Fig. 10(a), which causes a significant difference in the slopes for H I and H α. Note that the slope should be interpreted with caution, since there is a large scatter around this fit. The BTFR from McGaugh et al. (2000) is shown in orange for reference.

5 RESULTS

We use ancillary stellar data and observed H I data to examine the role local environment plays in our sample by comparing galaxy properties with respect to the location of the nearest neighbour. In addition, we examine the role large-scale environment plays by comparing galaxy properties with respect to location and orientation of the nearest cosmic web filament.

5.1 H I morphology and kinematics

An indication in our data that neighbours may have an impact on the morphology is shown in Fig. 11. Six out of 10 galaxies have the PA offset between the H I kinematic major axis and the optical photometric major axis by 30° or greater. For our sample, the more offset the PA the closer the galaxy is to its nearest neighbour. Another indication that neighbours may impact morphology and kinematics is the two dwarf irregular galaxies (1213496, 1180660) shown in Figs 6(a), A1, and A2. They have a separation in the sky of around 70 kpc and a difference in velocity of 5 km s^{-1}. For both galaxies, the H I velocity field of the outer disc shifts more towards

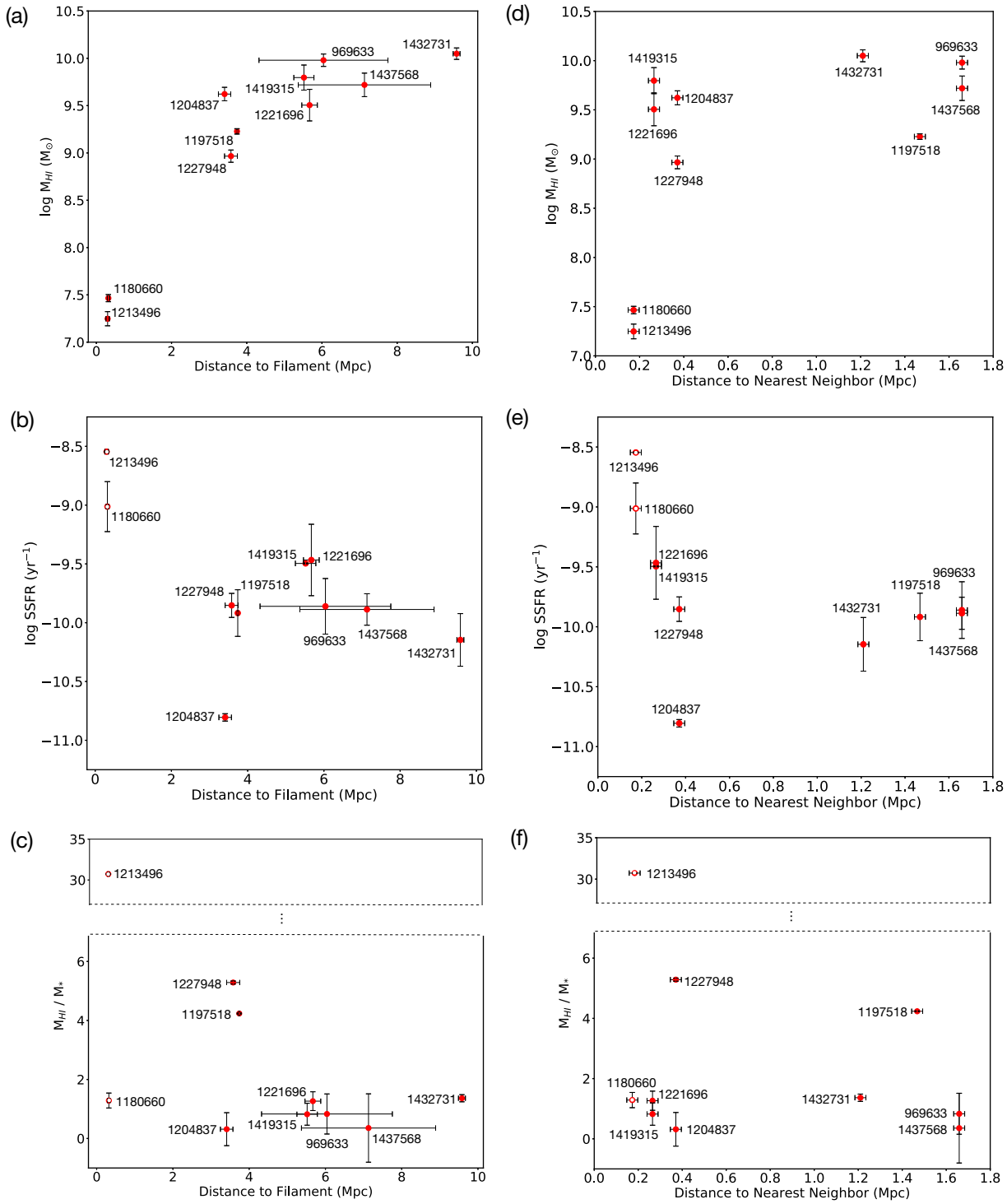

Figure 12. Relation of the galaxy properties and galaxy location. Fig. 12(a) shows the relation of H I mass and distance from the filament. Fig. 12(b) shows the relation of SSFR and distance from the filament. Fig. 12(c) shows the relation of gas fraction and distance from the filament. Figs 12(d), (e), and (f) show the stellar and the H I properties of our sample with respect to the nearest neighbour. Fig. 12(d) shows the relation of H I mass and distance from the nearest neighbour. Fig. 12(e) shows the relation of gas fraction and distance from the nearest neighbour. Fig. 12(f) shows the relation of SSFR and distance from the nearest neighbour. Open symbols are small galaxies with uncertain stellar masses.

being perpendicular to the H I major axis, indicative of a polar ring (Stanonik et al. 2009).

There are several galaxies in the sample with more prominent irregularities in their H I morphology and/or kinematics. For example, 1432731 has the most disturbed H I distribution, 1437568 has the most asymmetric H I morphology, 1180660 has the most shifted H I kinematics compared to the optical disc, and 1204837 has the most noticeable H I PA misalignment com-

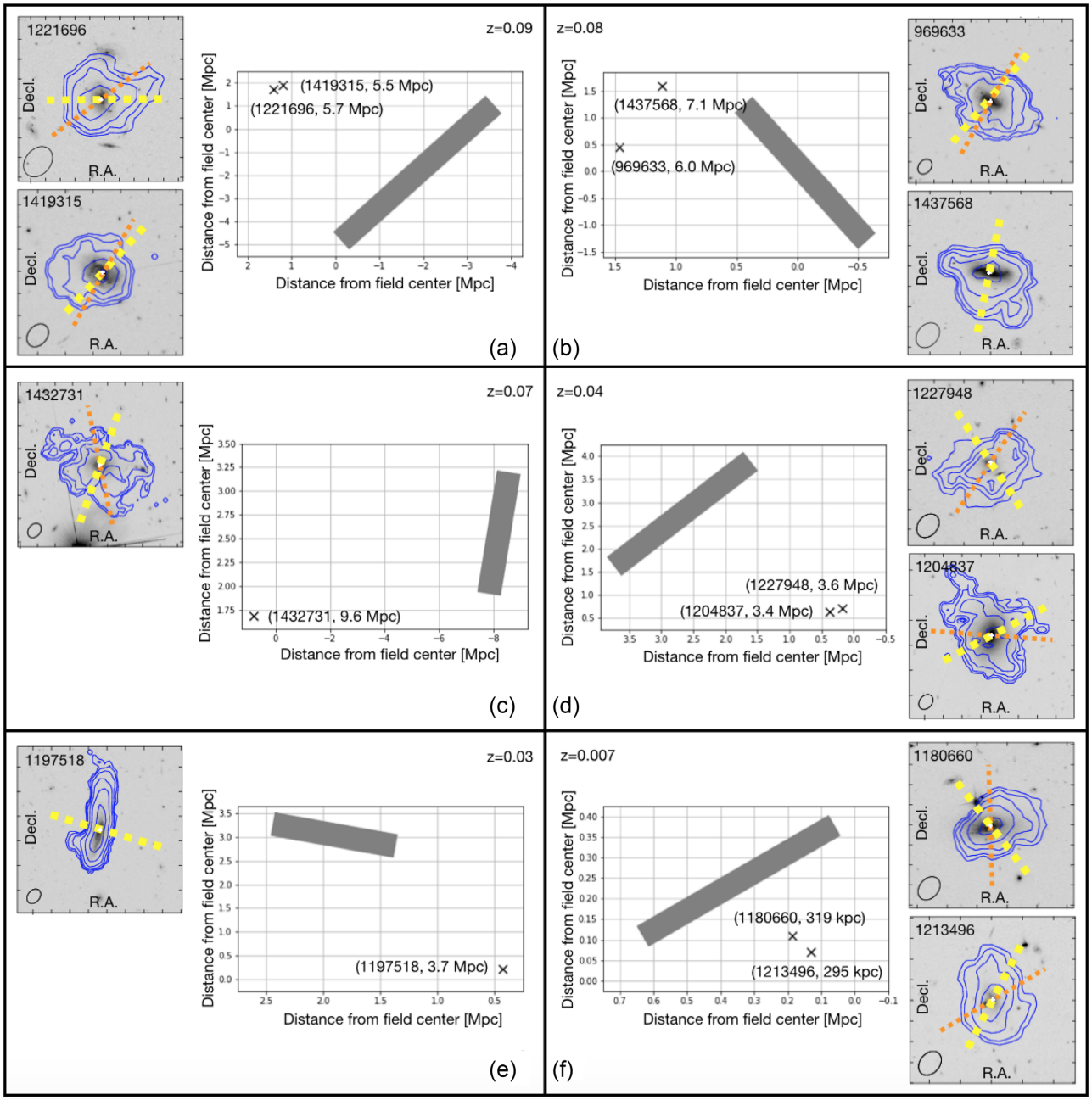

Figure 13. Relation of the galaxy spin vector and its nearest filament. In each panel (a–f), the grey line highlights the filament that is closest to each galaxy (shown with an *x*). The closest filament is calculated in three dimensions and is found by selecting the three closest critical points. Once the closest filament is identified, it is projected in two dimensions on to the sky as shown on the plots in each panel. The plot axes are distance from the field centre in Mpc (at the distance of the filament) and are comparable to right ascension and declination. The galaxy name and distance (in three dimensions) to the filament are shown next to each *x*. The redshift range is shown in the upper corner of each panel. Total H I intensity maps for the H I are shown along with the spin vectors for the H I gas (yellow-dashed line) and the spin vectors for the stellar disc (orange-dashed line). The axes are right ascension and declination.

pared to the optical PA plus two H I tails. Yet, the stellar discs of these galaxies appear to be undisturbed. There is no clear trend in H I irregularities with type, SFR, gas fraction, mass and environment of these galaxies, as they all span the entire range of the sample. With the optical images showing undisturbed stellar discs, the H I properties depict a more complex scenario, one that may include the accretion of gas from the surrounding environment.

5.2 Distance to cosmic web filaments

Both theory and observations suggest that large-scale structure impacts galaxy evolution in addition to known trends in local density. For example, observations show that at the same local density, redder, passive, and more massive galaxies are found closer to their filaments (Chen et al. 2017; Malavasi et al. 2017; Kraljic et al. 2018; Laigle et al. 2018). Studies on H I content have mixed results. Crone Odekon et al. (2018), using the ALFALFA catalogue,

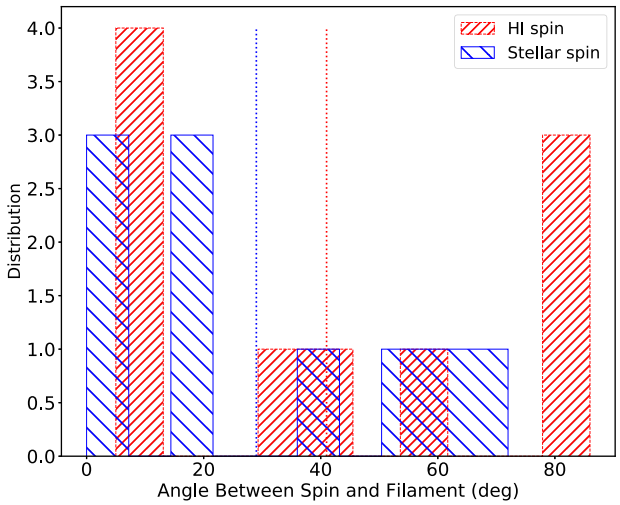

Figure 14. Angle between the galaxy spin vector and its nearest filament. The red shows the spin determined from the H I gas and the blue shows the spin determined from the stellar disc. The dotted lines are the average value for H I and stellar spin.

find that H I deficiency decreases as the distance from the filament increases and that most gas-rich galaxies are in small tendrils within voids. In contrast, Kleiner et al. (2017), using stacked spectra from the HIPASS catalogue, find that for galaxies with larger stellar mass log $M_*/M_\odot > 11$, the H I fraction in the sample 0.7 Mpc from filaments is higher than the H I fraction in galaxies far away from filaments. The study finds no difference in H I fraction between galaxies at 0.7 and 5 Mpc from filaments at smaller stellar mass log $M_*/M_\odot < 11$.

Our sample of galaxies lies within a range of 3D distances from the cosmic web. The two dwarf galaxies are around 300 kpc from a filament spine and the rest of the sample is from 3.4 to 9.6 Mpc from a filament spine. Since our low-mass sample is H I biased, it can be expected that our galaxies may be more isolated (Kreckel et al. 2012). Fig. 12(a) shows the H I mass increases with increasing distance from filaments. 1432731 is the most gas-rich galaxy in our sample with an H I mass of 1.1×10^{10} $M_\odot$. It has an H I diameter that is 71 kpc across and resides at the furthest distance in our sample at 9.6 Mpc from a filament spine. Fig. 12(b) shows the SSFR decreases with increasing distance from filaments. 1432731 has the lowest SSFR with respect to distance from filaments, with the exception of green valley galaxy 1204837. Since we have such a small sample, any of the relations shown should be considered only a hint of a trend at most. Lastly, the gas fraction in relation to distance from filamentary structure is shown in Fig. 12(c). Except for 1213496, 1227948, and 1197518, the gas fraction varies between 0.3 and 1.4 as a function of distance from filaments. Figs 12(d), (e), and (f) plot the same stellar and H I properties with respect to distances to the nearest neighbour and show no obvious trends.

5.3 Orientation to cosmic web filaments

Angular momentum is a key physical ingredient in galaxy formation and plays a crucial role in determining the history of a galaxy. Angular momentum has been a subject of classical investigations by Hoyle (1949) and Peebles (1969). The work of Doroshkevich (1970) and White (1984) led to a standard theory for the origin of angular momentum in the framework of hierarchical cosmological structure formation known as tidal torque theory. Galaxy dark matter haloes form in overdensities of the cosmic web by accreting material and smaller galaxies via filaments (Bond, Kofman & Pogosyan 1996). As large-scale structure collapses, galaxies acquire angular momentum and this process imprints alignments between the spin of galaxies and surrounding filaments. Low-mass galaxies assemble by accreting on to filaments, generating spins that align with filaments. High-mass galaxies assemble by merging along filaments, generating spins perpendicular to filaments. Extension of the work on tidal torque theory (Porciani et al. 2002) to non-linear environments (Codis et al. 2015) predicts this spin flip transition of haloes, as galaxies migrate along filaments and accumulate mass. This is also seen in increasingly detailed simulations (Kraljic et al. 2019), predicting the spin alignment of galaxies and haloes with respect to filaments, with spin flips occurring at a halo mass of 5×10^{11} h^{-1} to 5×10^{12} h^{-1} $M_\odot$.

Dark matter halo spin alignment has received much attention in the past, while studies of galaxy spin alignment have emerged only more recently. The dark matter halo spin flip transition is seen in both dark matter only simulations (Ganeshaiah Veena et al. 2018; Wang et al. 2018) and most hydrodynamical simulations (Codis et al. 2018; Ganeshaiah Veena et al. 2019). The case of galaxy spin alignment is less clear. The galaxy spin flip transition is seen in hydrodynamical simulations (Codis et al. 2018; Kraljic et al. 2019). In contrast, Ganeshaiah Veena et al. (2019) find a lack of detection of the galaxy spin flip transition and relate this to the filament thickness. The methods used in hydrodynamic simulations as well as the methods used to quantify the cosmic web may play a role in spin studies. Since Kraljic et al. (2019) use DisPerSE to identify the cosmic web in the SIMBA simulation (Davé et al. 2019), their results are directly comparable to our observations.

Observations of alignments between large-scale structure and the spin of galaxies show mixed results. Krolewski et al. (2019) find no clear evidence for alignment between galaxy spins and filament directions from kinematics using integral-field spectroscopy for 2700 galaxies from the MaNGA survey along with the Cosmic Web Reconstruction algorithm (Chen et al. 2016) to identify filaments. However, hints of the spin flip for galaxies have been identified in SDSS using shape as a proxy for galaxy spin (Tempel et al. 2013; Tempel & Libeskind 2013; Pahwa et al. 2016; Chen et al. 2019). More recently, Welker et al. (2019) detect mass dependent galactic spin alignments from kinematics using integral-field spectroscopy for 1278 galaxies from the SAMI survey, along with DisPerSE to characterize the cosmic web filaments.

We examine the spin vector alignments of our sample of galaxies with cosmic web filaments using the kinematic major axis of the H I gas and the photometric major axis of the stellar disc. The location of our sample of galaxies with respect to nearest filamentary spine based on the DisPerSE topological algorithm is shown in Fig. 13. We measure the galaxy angular momentum vector or spin vector from the PA of the major axis. The plane-of-sky projection of the spin vector is perpendicular to the PA of the major axis. The alignment between spin angle and filament angle is determined by taking the difference between the two apparent angles, both projected on to the sky.

Fig. 14 shows a histogram of the angle between the galaxy spin and filament. The red shows the spins determined from the H I gas and the blue shows the spins determined from the stellar disc. We follow the convention that if the angle is smaller than 45°, the alignment is referred to as parallel and conversely, if the angle is larger than 45°, the alignment is referred to as perpendicular. There is spread in the alignment angles for both the stellar and H I

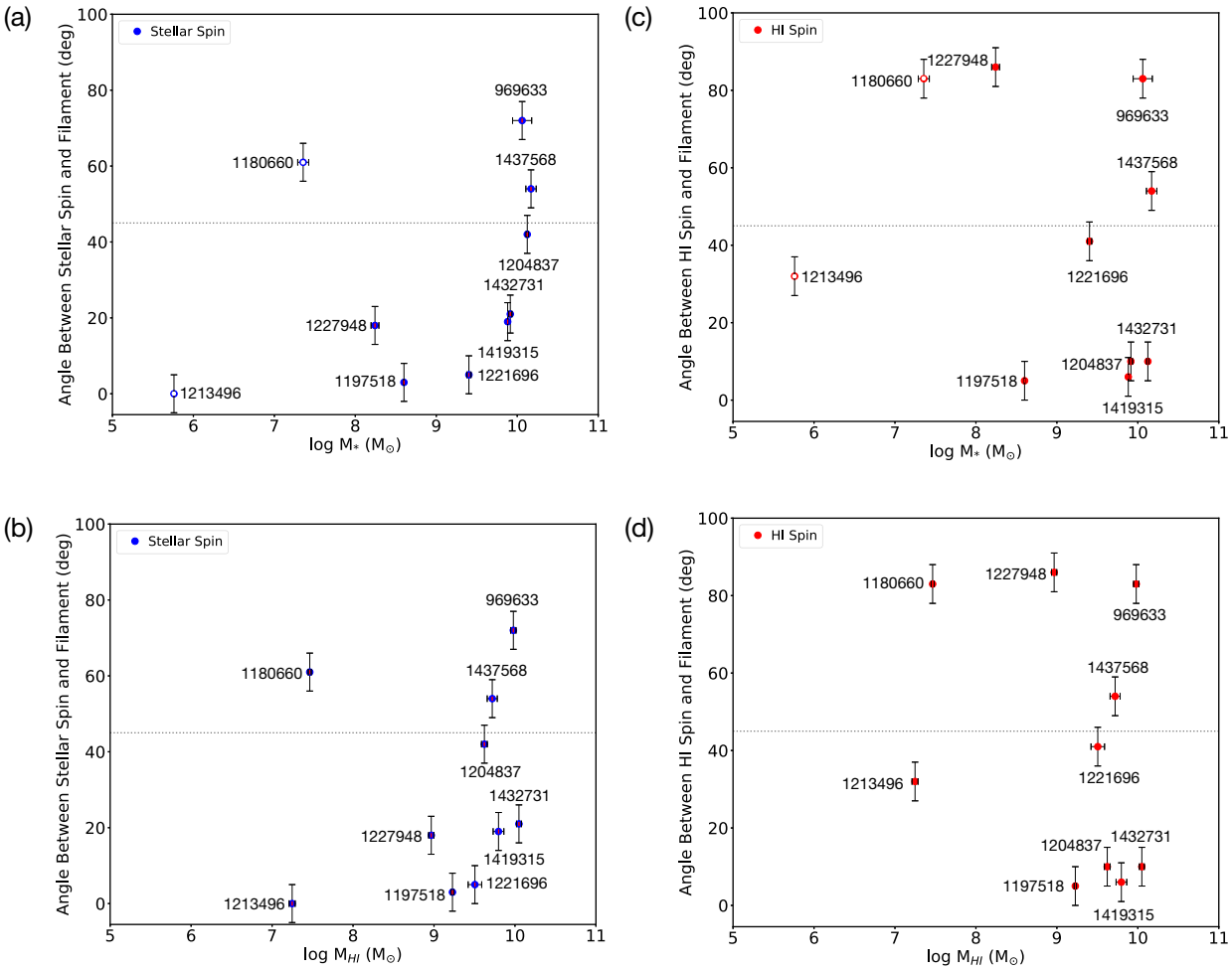

Figure 15. Relation of the spin-filament angle to mass. Fig. 15(a) shows the angle between the stellar spin and filament versus stellar mass. Fig. 15(b) shows the angle between the stellar spin and filament versus H I mass. Fig. 15(c) shows the angle between the H I spin and filament versus stellar mass. Fig. 15(d) shows the angle between the H I spin and filament versus H I mass. A dotted grey line is drawn at 45 deg. Open symbols are small galaxies with uncertain stellar masses.

components with a majority less than 45°. The average spin angle for the H I component is 41° and the average spin angle for the stellar component is 29°.

A transition between the aligned and perpendicular orientations of galaxy spins is found in some simulations, including the recent work by Kraljic et al. (2019). They find a transition in orientation at a stellar mass of $\sim 10^{10}$ $M_\odot$ and a transition in orientation at an H I mass of $\sim 10^{9.5}$ $M_\odot$, both based on the spin of the stellar component. Observationally, Welker et al. (2019) find a stellar transition mass from aligned to perpendicular orientations of galaxy spins bracketed between $10^{10.4}$ $M_\odot$ and $10^{10.9}$ $M_\odot$. They also compare their results to simulations finding that the transition mass varies with the mass scale used to define the filaments and that more refined filaments seem to lead to lower transition masses. Fig. 15 shows the spin-filament angles as a function of mass. If the three smallest galaxies are removed (1213496, 1180660, and 1227948), there seems to be a hint of transition in orientation just around $\sim 10^{10}$ $M_\odot$ in stellar mass (Fig. 15a) and a more bracketed hint of transition just below $\sim 10^{10}$ $M_\odot$ in H I mass (Fig. 15b), both based on the stellar spins. At most, these are marginal hints of the predicted trends. Figs 15(c) and (d) show a less convincing trend in transition for the H I spin in relation to stellar mass and H I mass. The results from our small sample are quite interesting and provide an opportunity to look at individual galaxies. However, a larger sample with better statistics is needed to draw firm conclusions and provide more profound insight into the alignment of spin vectors with filaments.

6 CONCLUSIONS

We present H I observations of 10 galaxies out to a redshift of 0.1 from the first epoch of CHILES. We find a large fraction (9 out of 10) of galaxies is somewhat disturbed, with large H I discs measuring the flat part of the rotation curve. The two dwarf irregular galaxies have disturbances in their outer discs that are indicative of polar rings and may be an indication that these two galaxies are gravitationally interacting. We compare the neutral and ionized gas for our sample of galaxies. It appears that H α rotation curves approach the flat part, making them useful for measuring dark matter content and TF studies.

We explore galaxy properties as a function of location to cosmic web filaments. We find that galaxy spins tend to be aligned with cosmic web filaments and a hint of the predicted transition mass

associated with the spin angle alignment. Our sample of galaxies lies within a range of distances from the cosmic web with the H I mass increases with increasing distance from filaments and SSFR decreases with increasing distance from filaments.

We utilize this small sample of nearby galaxies for a science verification study using our first 178 h. We find that our data follow known scaling relations and demonstrate the use of cosmic web filaments to study the impact of the large-scale environment on these systems. With the full 1000 h of the CHILES survey, we will be able to further study galaxy properties and orientation with respect to the cosmic web with images of close to 400 galaxies, using a broader mass sample, over the continuous redshift range ($0 < z < 0.45$) of the entire survey.

ACKNOWLEDGEMENTS

We would like to thank reviewer E. Tempel for very useful and constructive comments. We also thank K. Kraljic for very helpful comments on the paper. We would like to thank the entire CHILES collaboration. We additionally thank Steve Crawford and Ralf Kotulla for their assistance with SALT data reduction. We would also like to thank K. Vinsen and E. da Cunha who ran the SED fitting on the G10/COSMOS v05 catalogue with MAGPHYS. JD acknowledges support by the National Science Foundation (NSF) Graduate Research Fellowship Program under grant no. DGE-1747503 and NASA under award no. NNX15AJ12H issued through Wisconsin Space Grant Consortium. DJP and NL acknowledge partial support from NSF grant no. AST 1412578. JMvdH acknowledges support from the European Research Council under the European Union's Seventh Framework Programme (FP/2007-2013)/ERC grant agreement no. 291531. MY and HBG acknowledge support from NSF grant no. AST 1412843. This work is in part supported by the NSF under grant no. AST 141302 to Columbia University. Support for this work is also provided by the NSF through award SOSP 18_3133 from the National Radio Astronomy Observatory (NRAO). The NRAO is a facility of the NSF operated under cooperative agreement by Associated Universities, Inc.

This research made use of ASTROPY, a community-developed core PYTHON package for Astronomy (Astropy Collaboration 2013). Rotation curve overlays are made using MATPLOTLIB (Hunter 2007).

Facilities: NED, SALT, VLA software: ASTROPY, CASA, IDL, IRAF, PYSALT

REFERENCES

Abazajian K. N. et al., 2009, ApJS, 182, 543
Andrews S. K., Driver S. P., Davies L. J. M., Kafle P. R., Robotham A. S. G., Wright A. H., 2017, MNRAS, 464, 1569
Aragon Calvo M. A., Neyrinck M. C., Silk J., 2019, Open J. Astrophys., 2, 7
Athanassoula E., Bureau M., 1999, ApJ, 522, 699
Baldwin J. A., Phillips M. M., Terlevich R., 1981, PASP, 93, 5
Barnes D. G. et al., 2001, MNRAS, 322, 486
Belfiore F. et al., 2017, MNRAS, 469, 151
Bond J. R., Kofman L., Pogosyan D., 1996, Nature, 380, 603
Catinella B. et al., 2012, A&A, 544, A65
Chen Y.-C., Ho S., Brinkmann J., Freeman P. E., Genovese C. R., Schneider D. P., Wasserman L., 2016, MNRAS, 461, 3896
Chen Y.-C. et al., 2017, MNRAS, 466, 1880
Chen Y.-C., Ho S., Blazek J., He S., Mandelbaum R., Melchior P., Singh S., 2019, MNRAS, 485, 2492
Chung A., van Gorkom J. H., Kenney J. D. P., Crowl H., Vollmer B., 2009, AJ, 138, 1741
Codis S., Pichon C., Pogosyan D., 2015, MNRAS, 452, 3369
Codis S., Jindal A., Chisari N. E., Vibert D., Dubois Y., Pichon C., Devriendt J., 2018, MNRAS, 481, 4753
Crawford S. M. et al., 2010, Proc. SPIE, 7737, 773725
Crone Odekon M., Hallenbeck G., Haynes M. P., Koopmann R. A., Phi A., Wolfe P.-F., 2018, ApJ, 852, 142
Da Cunha E., Charlot S., Elbaz D., 2008, MNRAS, 388, 1595
Davé R., Anglés-Alcázar D., Narayanan D., Li Q., Rafieferantsoa M. H., Appleby S., 2019, MNRAS, 486, 2827
Davies L. J. M. et al., 2015, MNRAS, 447, 1014
Dénes H., Kilborn V. A., Koribalski B. S., 2014, MNRAS, 444, 667
Dodson R. et al., 2016, Astron. Comput., 14, 8
Dopita M. A., Kewley L. J., Sutherland R. S., Nicholls D. C., 2016, Ap&SS, 361, 61
Doroshkevich A. G., 1970, Astrophysics, 6, 320
Fernández X. et al., 2013, ApJ, 770, L29
Fernández X. et al., 2016, ApJ, 824, L1
Florido E., Zurita A., Pérez I., Pérez-Montero E., Coelho P. R. T., Gadotti D. A., 2015, A&A, 584, A88
Ganeshaiah Veena P., Cautun M., van de Weygaert R., Tempel E., Jones B. J. T., Rieder S., Frenk C. S., 2018, MNRAS, 481, 414
Ganeshaiah Veena P., Cautun M., Tempel E., van de Weygaert R., Frenk C. S., 2019, MNRAS, 487, 1607
Giovanelli R. et al., 2005, AJ, 130, 2598
Haynes M. P., Giovanelli R., 1984, AJ, 89, 758
Haynes M. P. et al., 2011, AJ, 142, 170
Heald G. et al., 2011, A&A, 526, A118
Hess K. M. et al., 2019, MNRAS, 484, 2234
Hoyle F., 1949. Central Air Documents Office, Dayton OH
Huang S., Haynes M. P., Giovanelli R., Brinchmann J., 2012, ApJ, 756, 113
Hunter D. A. et al., 2012, AJ, 144, 134
Jütte E., van Eymeren J., Jog C. J., Dettmar R. J., Stein Y., 2013, Mem. Soc. Astron. Ital. Suppl., 25, 55
Kauffmann G. et al., 2003, MNRAS, 341, 54
Kereš D., Katz N., Weinberg D. H., Davé R., 2005, MNRAS, 363, 2
Kleiner D., Pimbblet K. A., Jones D. H., Koribalski B. S., Serra P., 2017, MNRAS, 466, 4692
Koekemoer A. M. et al., 2007, ApJS, 172, 196
Kraljic K. et al., 2018, MNRAS, 474, 547
Kraljic K., Dave R., Pichon C., 2019, preprint (arXiv:1906.01623)
Kreckel K., Platen E., Aragón-Calvo M. A., van Gorkom J. H., van de Weygaert R., van der Hulst J. M., Beygu B., 2012, AJ, 144, 16
Krolewski A., Ho S., Chen Y.-C., Chan P. F., Tenneti A., Bizyaev D., Kraljic K., 2019, ApJ, 876, 52
Kuutma T., Tamm A., Tempel E., 2017, A&A, 600, L6
Laigle C. et al., 2018, MNRAS, 474, 5437
Lelli F., McGaugh S. S., Schombert J. M., Desmond H., Katz H., 2019, MNRAS, 484, 3267
Libeskind N. I. et al., 2018, MNRAS, 473, 1195
Luber N., van Gorkom J. H., Hess K. M., Pisano D. J., Fernandez X., Momjian E., 2019, AJ, 157, 254
Maddox N., Hess K. M., Obreschkow D., Jarvis M. J., Blyth S. L., 2015, MNRAS, 447, 1610
Malavasi N. et al., 2017, MNRAS, 465, 3817
Marino R. A. et al., 2013, A&A, 559, A114
Martinsson T. P. K., Verheijen M. A. W., Bershady M. A., Westfall K. B., Andersen D. R., Swaters R. A., 2016, A&A, 585, A99
Martin D. C. et al., 2005, ApJ, 619, L1
Massey R., Stoughton C., Leauthaud A., Rhodes J., Koekemoer A., Ellis R., Shaghoulian E., 2010, MNRAS, 401, 371
McGaugh S. S., Schombert J. M., Bothun G. D., de Blok W. J. G., 2000, ApJ, 533, L99
McMullin J. P., Waters B., Schiebel D., Young W., Golap K., 2007, in Shaw R. A., Hill F., Bell D. J., eds, ASP Conf. Ser. Vol. 376, Astronomical Data Analysis Software and Systems XVI. Astron. Soc. Pac., San Francisco, p. 127
Pahwa I. et al., 2016, MNRAS, 457, 695
Peebles P. J. E., 1969, ApJ, 155, 393

Pisano D. J., Kobulnicky H. A., Guzmán R., Gallego J., Bershady M. A., 2001, AJ, 122, 1194
Planck Collaboration et al., 2018, preprint (arXiv:1807.06205)
Porciani C., Dekel A., Hoffman Y., 2002, MNRAS, 332, 325
Sánchez Almeida J., Elmegreen B. G., Muñoz-Tuñón C., Elmegreen D. M., 2014, A&A Rev., 22, 71
Sancisi R., Fraternali F., Oosterloo T., van der Hulst T., 2008, A&A Rev., 15, 189
Schiminovich D. et al., 2007, ApJS, 173, 315
Scoville N. et al., 2007, ApJS, 172, 1
Serra P., Jurek R., Flöer L., 2012, PASA, 29, 296
Serra P. et al., 2015, MNRAS, 448, 1922
Sofue Y., Tutui Y., Honma M., Tomita A., Takamiya T., Koda J., Takeda Y., 1999, ApJ, 523, 136
Sousbie T., 2011, MNRAS, 414, 350
Stanonik K., Platen E., Aragón-Calvo M. A., van Gorkom J. H., van de Weygaert R., van der Hulst J. M., Peebles P. J. E., 2009, ApJ, 696, L6
Swaters R. A., van Albada T. S., van der Hulst J. M., Sancisi R., 2002, A&A, 390, 829
Tempel E., Libeskind N. I., 2013, ApJ, 775, L42
Tempel E., Stoica R. S., Saar E., 2013, MNRAS, 428, 1827
Tully R. B., Fisher J. R., 1977, A&A, 500, 105
Van der Hulst J. M., van Albada T. S., Sancisi R., 2001, in Hibbard J. E., Rupen M., van Gorkom J. H., eds, ASP Conf. Ser. Vol. 240, Gas and Galaxy Evolution. Astron. Soc. Pac., San Francisco, p. 451
Verheijen M. A. W., Sancisi R., 2001, A&A, 370, 765
Verheijen M. A. W., 2001, ApJ, 563, 694
Walter F., Brinks E., de Blok W. J. G., Bigiel F., Kennicutt Robert C. J., Thornley M. D., Leroy A., 2008, AJ, 136, 2563
Wang J., Koribalski B. S., Serra P., van der Hulst T., Roychowdhury S., Kamphuis P., Chengalur J. N., 2016, MNRAS, 460, 2143
Wang P., Guo Q., Kang X., Libeskind N. I., 2018, ApJ, 866, 138
Welker C. et al., 2019, MNRAS, 2470
White S. D. M., 1984, ApJ, 286, 38
Zhang K. et al., 2017, MNRAS, 466, 3217

APPENDIX A: FIGURES FOR INDIVIDUAL GALAXIES

We present figures for individual galaxies (Figs A1–A10).

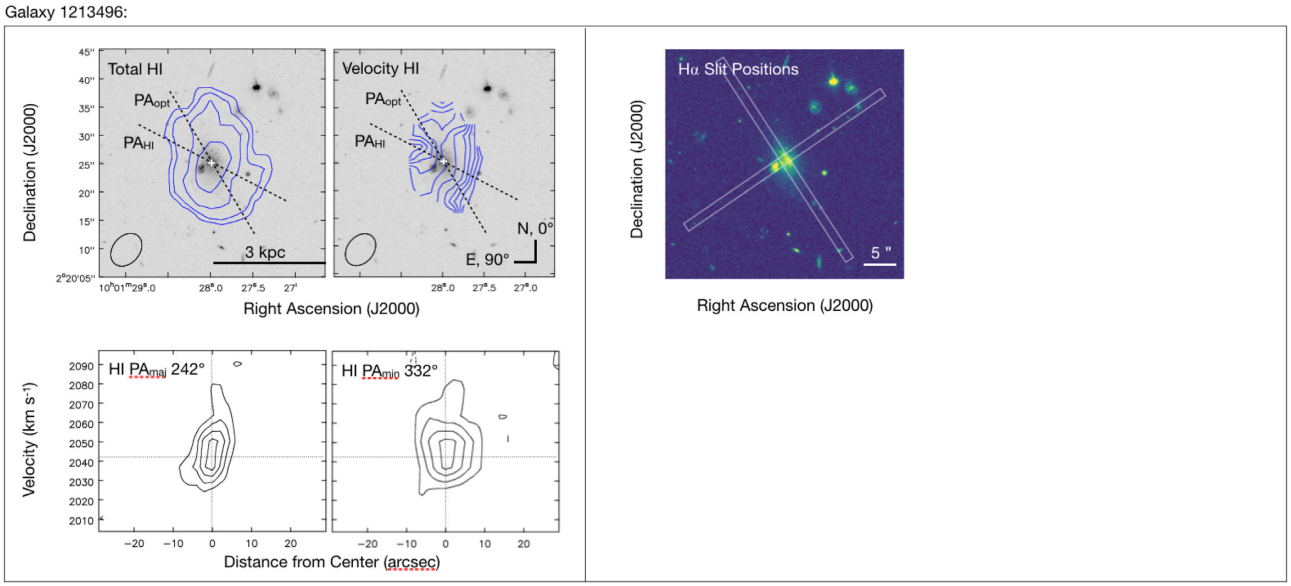

Figure A1. Properties for galaxy 1213496. Detailed descriptions can be found in Section 3.6. H I PV diagrams: 76 (rms) × −4, −2 (dashed), 2, 4, 6, 8 μJy beam^{-1}; H I total integrated flux: 6.6 (2σ, 13.3 km s^{-1} channel), 13.2, 26.5, 53.0 × 10^{19} cm^{-2}; H I velocity field: 2041 (system) ± 5 km s^{-1}; H I PA: H I major axis PA is taken from the receding side. The global H I profile is shown in Fig. 3. No H α is detected for this galaxy.

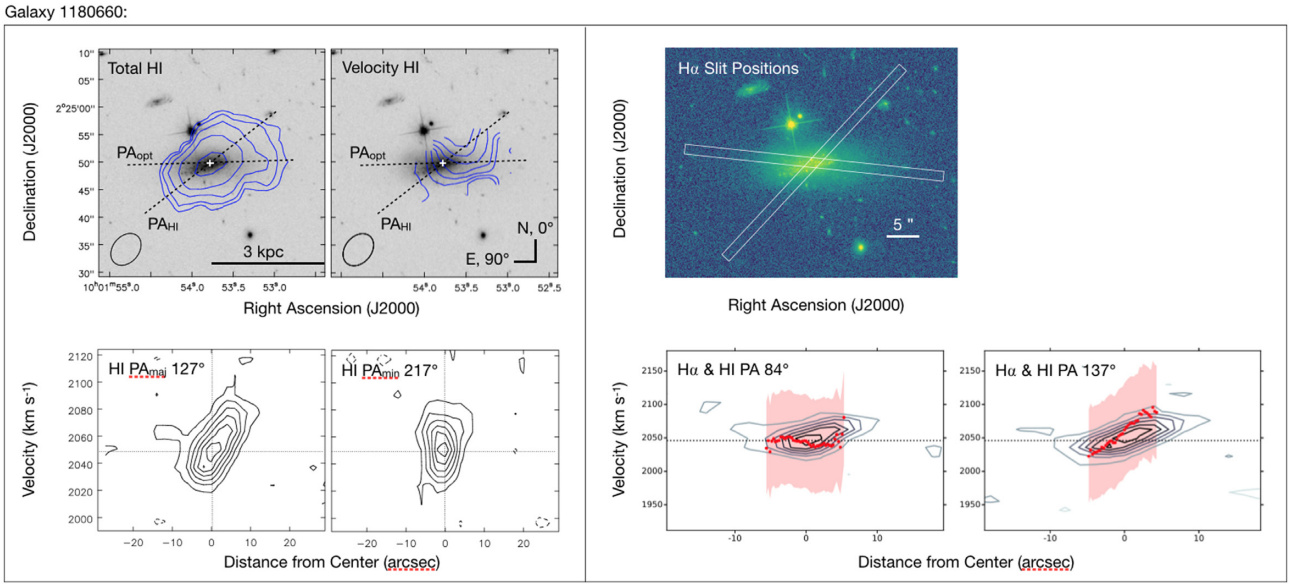

Figure A2. Properties for galaxy 1180660. Detailed descriptions can be found in Section 3.6. H I PV diagrams: 76 (rms) × −4, −2 (dashed), 2, 4, 6, 8, 10, 12 μJy beam^{-1}; H I total integrated flux: 6.6 (2σ, 13.3 km s^{-1} channel), 13.2, 26.5, 53.0, 106.0 × 10^{19} cm^{-2}; H I velocity field: 2046 (system) ± 3 km s^{-1}; H I PA: H I major axis PA is taken from the receding side. The global H I profile is shown in Fig. 3. H α is represented by the red points, and the red shaded region is the SALT velocity resolution (∼ 70 km s^{-1}), taken here as the uncertainty.

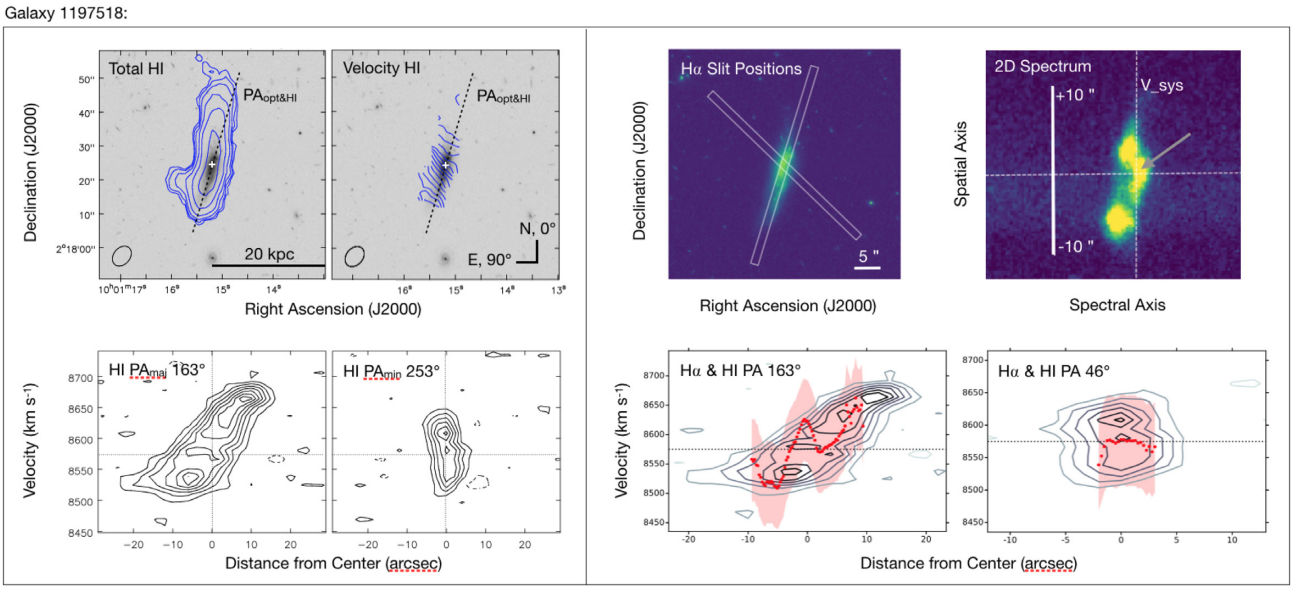

Figure A3. Properties for galaxy 1197518. Detailed descriptions can be found in Section 3.6. H I PV diagrams: 74 (rms) × −4, −2 (dashed), 2, 4, 6, 8, 10, 12, 14 μJy beam^{-1}; H I total integrated flux: 6.8 (2σ, 13.6 km s^{-1} channel), 13.6, 27.3, 54.6, 109.0 × 10^{19} cm^{-2}; H I velocity field: 8575 (system) ± 10 km s^{-1}; H I PA: H I major axis PA is taken from the receding side. The global H I profile is shown in Fig. 3. H α is represented by the red points, and the red shaded region is the SALT velocity resolution (∼70 km s^{-1}), taken here as the uncertainty. The upper rightmost image is the 2D SALT spectrum, showing the H α emission line. The emission line is poorly fit by a single Gaussian and results in the H α rotation curve kink, due to the clump indicated by the grey arrow on the redward side of the normal rotation component. This clump could also be gas in non-circular motion due to the bar, and in front so we do not see the corresponding back side due to extinction.

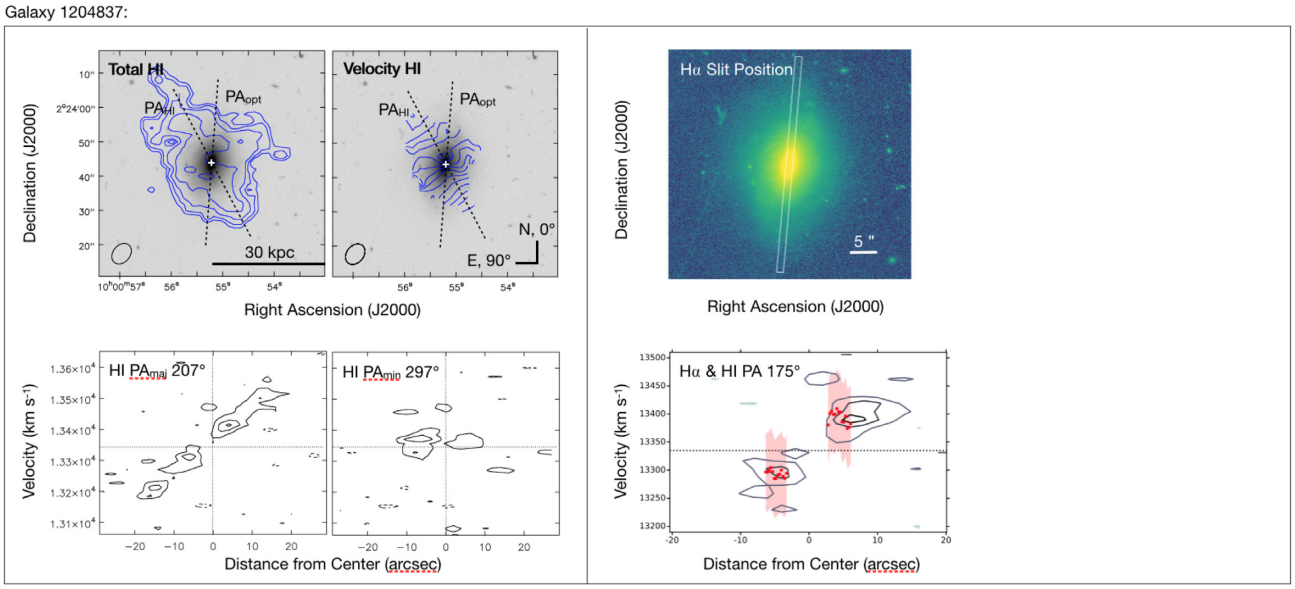

Figure A4. Properties for galaxy 1204837. Detailed descriptions can be found in Section 3.6. H I PV diagrams: 79 (rms) × −4, −2 (dashed), 2, 4, 6 μJy beam^{-1}; H I total integrated flux: 7.5 (2σ, 13.8 km s^{-1} channel), 14.9, 29.8, 59.7, 119.0 × 10^{19} cm^{-2}; H I velocity field: 13335 (system) ± 20 km s^{-1}; H I PA: H I major axis PA is taken from the receding side. The global H I profile is shown in Fig. 3. Hα is represented by the red points, and the red shaded region is the SALT velocity resolution ($\sim$ 70 km s^{-1}), taken here as the uncertainty.

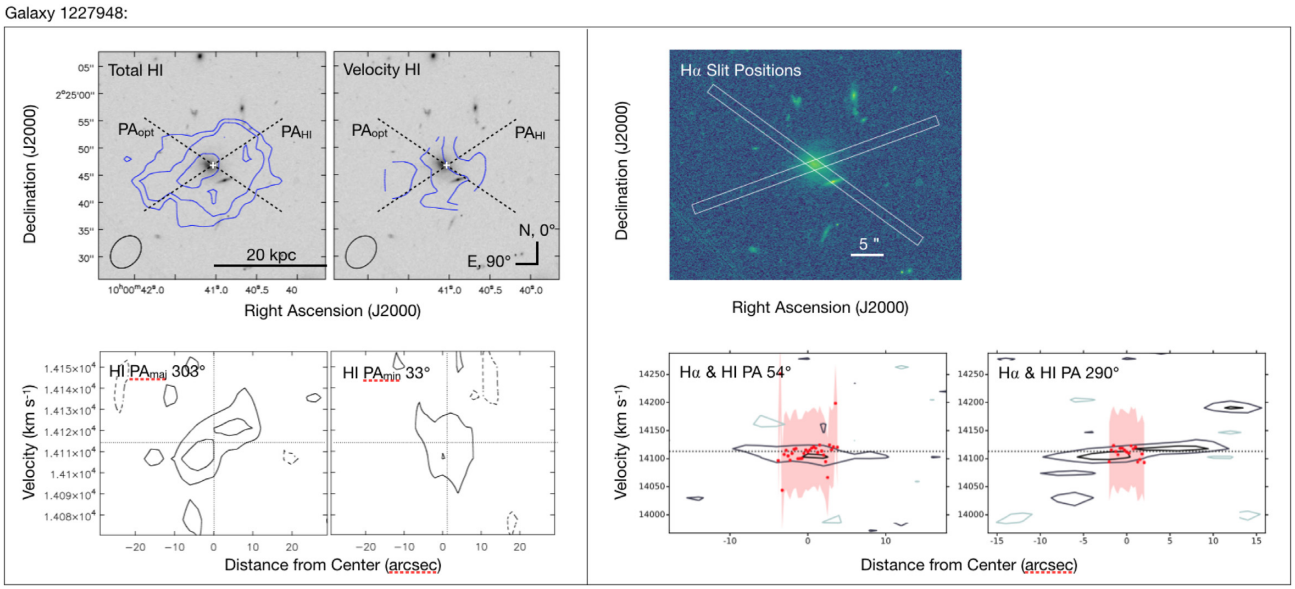

Figure A5. Properties for galaxy 1227948. Detailed descriptions can be found in Section 3.6. H I PV diagrams: 79 (rms) × −4, −2 (dashed), 2, 4 μJy beam^{-1}; H I total integrated flux: 7.5 (2σ, 13.8 km s^{-1} channel), 15.1, 30.1 × 10^{19} cm^{-2}; H I velocity field: 14113 (system) ± 5 km s^{-1}; H I PA: H I major axis PA is taken from the receding side. The global H I profile is shown in Fig. 3. H α is represented by the red points, and the red shaded region is the SALT velocity resolution ($\sim$ 70 km s^{-1}), taken here as the uncertainty.

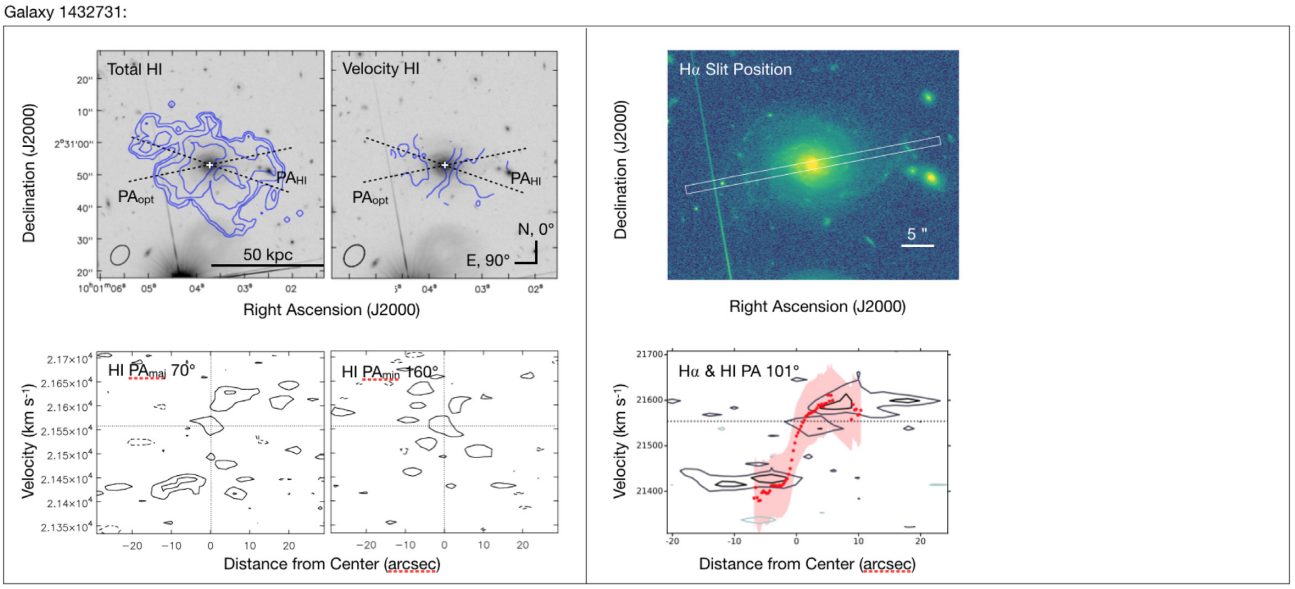

Figure A6. Properties for galaxy 1432731. Detailed descriptions can be found in Section 3.6. H I PV diagrams: 86 (rms) × −4, −2 (dashed), 2, 4 μJy beam^{-1}; H I total integrated flux: 8.5 (2σ, 14.1 km s^{-1} channel), 17.0, 34.1, 68.2 × 10^{19} cm^{-2}; H I velocity field: 21554 (system) ± 50 km s^{-1}; H I PA: H I major axis PA is taken from the receding side. The global H I profile is shown in Fig. 3. H α is represented by the red points, and the red shaded region is the SALT velocity resolution (∼ 70 km s^{-1}), taken here as the uncertainty. Note: The system velocity V_{sys} is indicated with the horizontal dotted line in the PV diagrams and is taken as the velocity value at the optical centre of the velocity field. For G146, this value appears higher than where the system velocity is expected to fall on the PV diagrams, at the centre between the maximum velocity of the rising and declining parts of the H I emission.

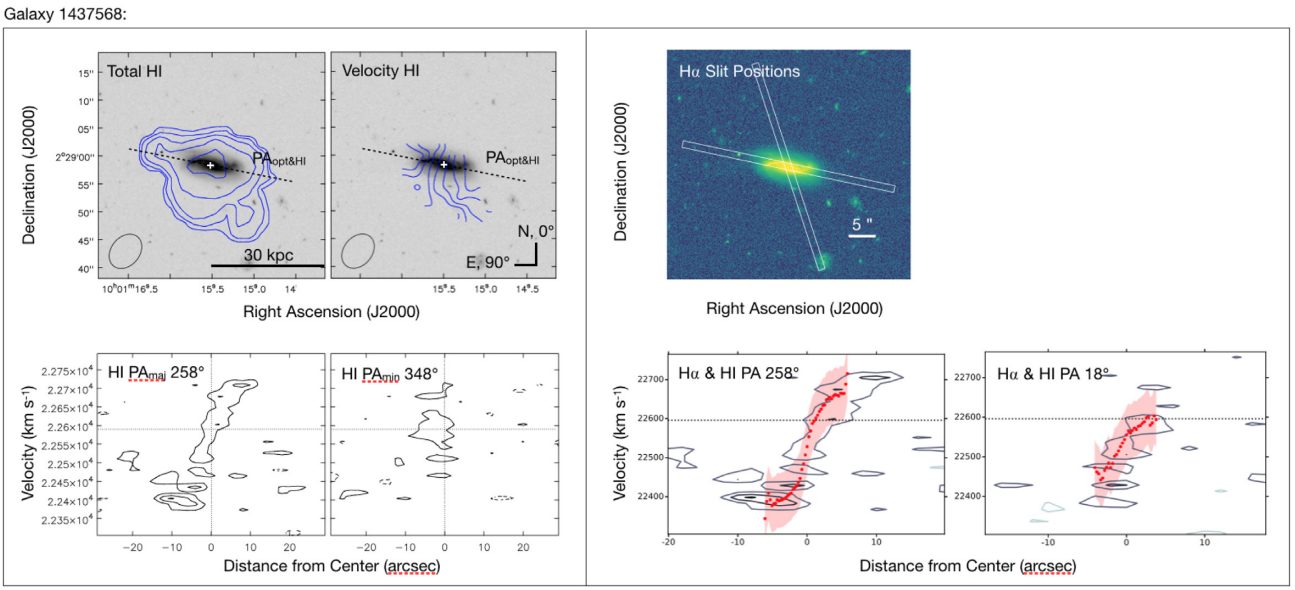

Figure A7. Properties for galaxy 1437568. Detailed descriptions can be found in Section 3.6. H I PV diagrams: 86 (rms) × −4, −2 (dashed), 2, 4, 6 μJy beam^{-1}; H I total integrated flux: 8.6 (2σ, 14.1 km s^{-1} channel), 17.3, 34.6, 69.1, 138 .0 × 10^{19} cm^{-2}; H I velocity field: 22596 (system) ± 30 km s^{-1}; H I PA: H I major axis PA is taken from the receding side. The global H I profile is shown in Fig. 3. H α is represented by the red points, and the red shaded region is the SALT velocity resolution (∼70 km s^{-1}), taken here as the uncertainty. Note: The system velocity V_{sys} is indicated with the horizontal dotted line in the PV diagrams and is taken as the velocity value at the optical centre of the velocity field. For 1437568, this value appears higher than where the system velocity is expected to fall on the PV diagrams, at the centre between the maximum velocity of the rising and declining parts of the H I emission.

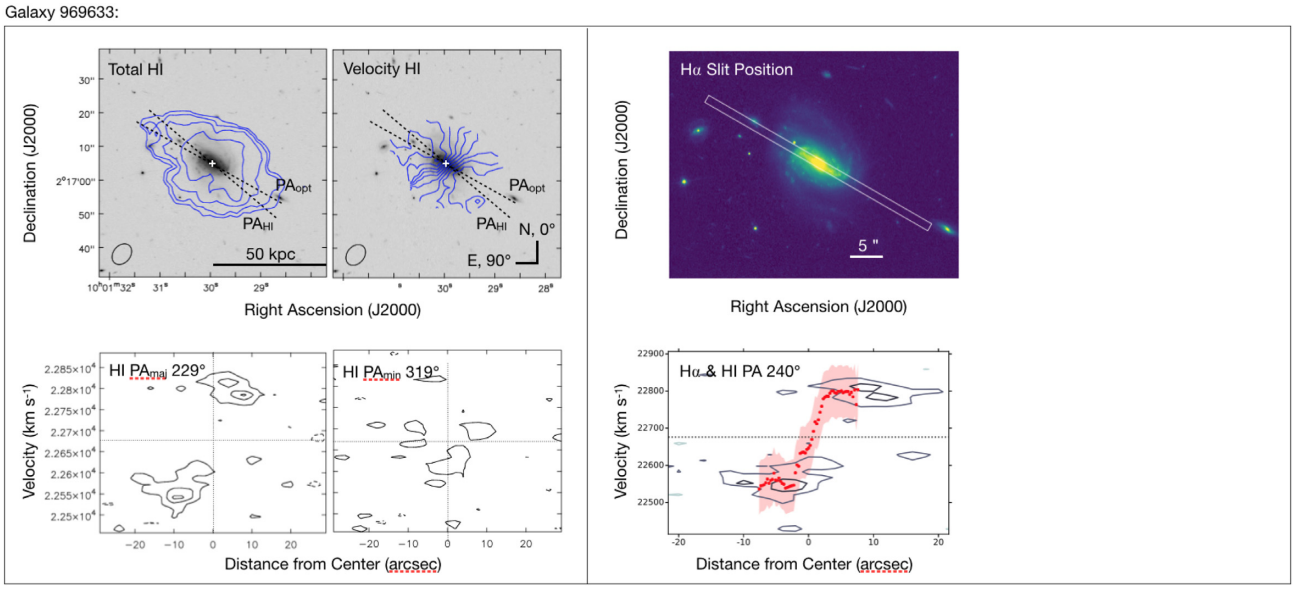

Figure A8. Properties for galaxy 969633. Detailed descriptions can be found in Section 3.6. H I PV diagrams: 86 (rms) × −4, −2 (dashed), 2, 4, 6 μJy beam^{-1}; H I total integrated flux: 8.6 (2σ, 14.1 km s^{-1} channel), 17.3, 34.6, 69.1 × 10^{19} cm^{-2}; H I velocity field: 22676 (system) ± 25 km s^{-1}; H I PA: H I major axis PA is taken from the receding side. The global H I profile is shown in Fig. 3. H α is represented by the red points, and the red shaded region is the SALT velocity resolution (∼70 km s^{-1}), taken here as the uncertainty.

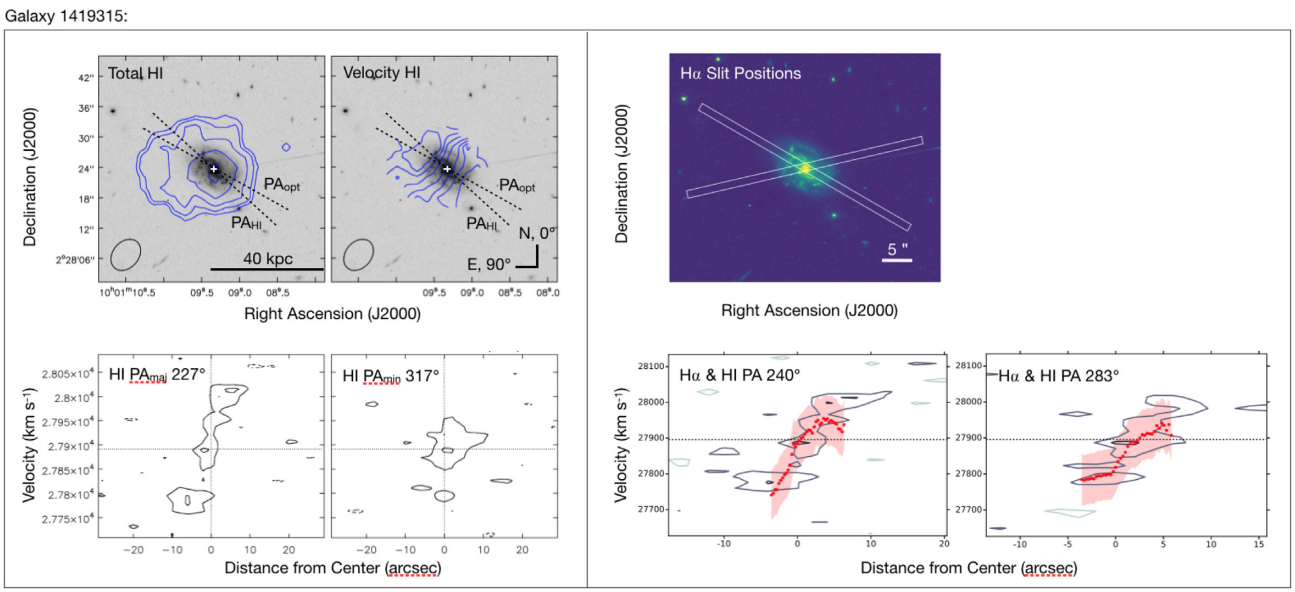

Figure A9. Properties for galaxy 1419315. Detailed descriptions can be found in Section 3.6. H I PV diagrams: 83 (rms) × −4, −2 (dashed), 2, 4 μJy beam^{-1}; H I total integrated flux: 8.8 (2σ, 14.3 km s^{-1} channel), 17.6, 35.3, 70.5 × 10^{19} cm^{-2}; H I velocity field: 27896 (system) ± 30 km s^{-1}; H I PA: H I major axis PA is taken from the receding side. The global H I profile is shown in Fig. 3. H α is represented by the red points, and the red shaded region is the SALT velocity resolution (∼70 km s^{-1}), taken here as the uncertainty.

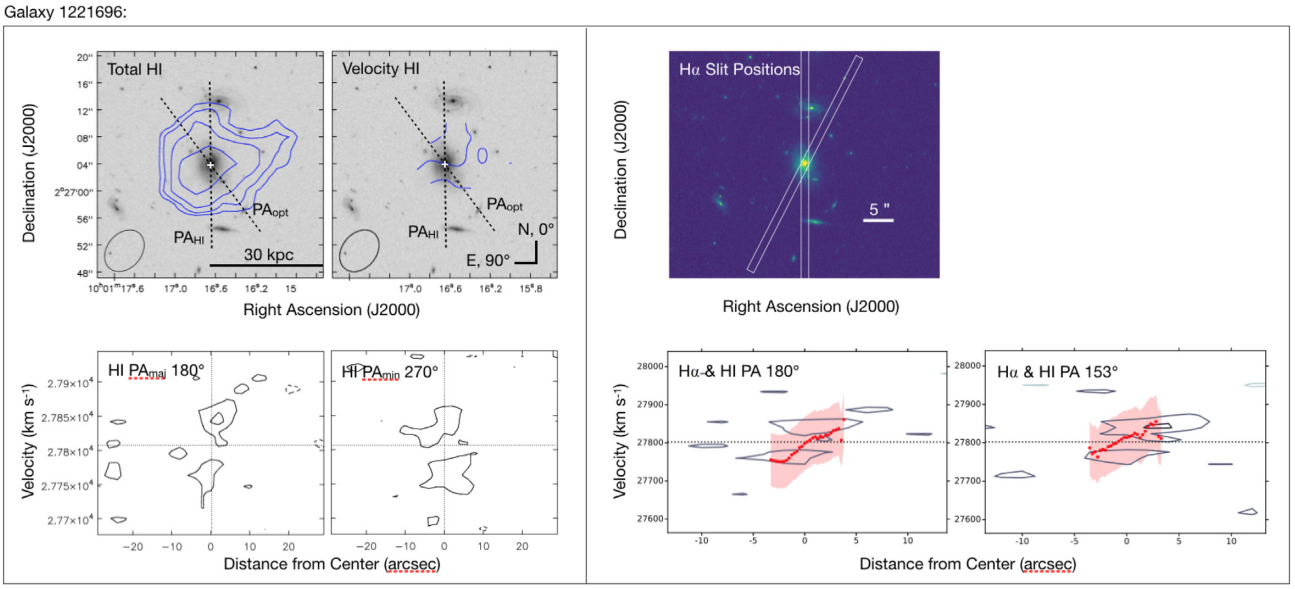

Figure A10. Properties for galaxy 1221696. Detailed descriptions can be found in Section 3.6. PV diagrams: 83 (rms) × −4, −2 (dashed), 2, 4 μJy beam^{-1}; H I total integrated flux: 8.8 (2σ, 14.3 km s^{-1} channel), 17.6, 35.2, 70.5 × 10^{19} cm^{-2}; H I velocity field: 27802 (system) ± 30 km s^{-1}; H I PA: H I major axis PA is taken from the receding side. The global H I profile is shown in Fig. 3. H α is represented by the red points, and the red shaded region is the SALT velocity resolution (∼70 km s^{-1}), taken here as the uncertainty.

This paper has been typeset from a TEX/LATEX file prepared by the author.